creative commons

COMMONS DEED

저작자표시-비영리-변경금지 2.0 대한민국

이용자는 아래의 조건을 따르는 경우에 한하여 자유롭게

- 이 저작물을 복제, 배포, 전송, 전시, 공연 및 방송할 수 있습니다.

다음과 같은 조건을 따라야 합니다:

저작자표시. 귀하는 원저작자를 표시하여야 합니다.

비영리. 귀하는 이 저작물을 영리 목적으로 이용할 수 없습니다.

변경금지. 귀하는 이 저작물을 개작, 변형 또는 가공할 수 없습니다.

- 귀하는, 이 저작물의 재이용이나 배포의 경우, 이 저작물에 적용된 이용허락조건을 명확하게 나타내어야 합니다.
- 저작권자로부터 별도의 허가를 받으면 이러한 조건들은 적용되지 않습니다.

저작권법에 따른 이용자의 권리는 위의 내용에 의하여 영향을 받지 않습니다.

이것은 이용허락규약(Legal Code)을 이해하기 쉽게 요약한 것입니다.

Disclaimer

dCollection

이학박사 학위논문

Optical spectroscopic studies on magnetic excitation in pyrochlore iridates

파이로클로로 이리듐 산화물에서의 자기적 들뜸 현상에 대한 분광학 연구

2021 년 8 월

서울대학교 대학원

물리천문학부

손 재 석

Optical spectroscopic studies on magnetic excitation in pyrochlore iridates

Jaeseok Son

Supervised by

Professor Tae Won Noh

A Dissertation submitted to the Faculty of Seoul National University in Partial Fulfillment of the Requirements for the Degree of Doctor of Philosophy

August 2021

Department of Physics and Astronomy

Graduate School

Seoul National University

Optical spectroscopic studies on magnetic excitation in pyrochlore iridates

파이로클로로 이리듐 산화물에서의 자기적 들뜸 현상에 대한 분광학 연구

지도교수 노 태 원

이 논문을 이학박사 학위논문으로 제출함
2021 년 6 월

서울대학교 대학원
물리천문학부
손 재 석

손재석의 이학박사 학위논문을 인준함
2021 년 7 월

위 원 장	양 범 정
부위원장	노 태 원
위 원	최 현 용
위 원	이 지 은
위 원	문 순 재

Contents

List of figures…….iv

List of Tables…….xi

Abstracts…….. xii

1 Introduction……. 1

1.1 Iridate and Jeff=1/2 state…….....2

1.2 Pyrochlore iridates with All-in-all-out magnetism…….3

1.3 Topology in pyrochlore iridates……..4

1.4 Outline of Thesis…… 5

2 Experimental Methods……7

2.1 Introduction to optical spectroscopy……..8

2.2 Spectroscopic ellipsometry……... 8

2.3 Fourier transform infrared spectroscopy…… 9

2.4 Raman spectroscopy……... 11

3 Result and Discussion I: IR spectroscopy…….. 13

3.1 Introduction…….. 14

3.1.1 Brief history of optical studies in 5d pyrochlore materials……..14

3.1.2 Spin-phonon coupling in 5d TMO……...14

3.2 Experimental details…….....16

3.3 Spectroscopic investigation……..17

3.3.1 Optical phonon spectral results……17

3.3.2 Lorentzian fitting…….18

3.4 Theoretical calculation……..21

3.4.1 DFT calculations……..21

3.4.2 Tight biding model calculations……...29

3.5 Conclusion……34

4 Result and Discussion II: Raman spectroscopy…….35

4.1 Introduction…….. 36

4.1.1 Brief history of magnon topology in pyrochlore lattice system……36

4.1.2 Brief history of magnon studies Raman spectroscopy……..38

4.2 Experimental details……..... 39

4.3 Spectroscopic investigation……..40

4.3.1 Temperature dependent Raman spectra……40

4.3.2 Spin-wave dispersion of pyrochlore iridates……45

4.3.3 Single-magnon scattering mechanism in pseudospin J_{eff}=1/2 configuration..49

4.4 Theoretical calculation …….54

4.4.1 Tight-binding model estimations …….....54

4.4.2 Spin-phonon coupling in Raman spectroscopy……56

4.5 Conclusion ……...63

5 Summary and Concluding Remarks ……..65

6 References……. 67

7 Appendix ……...72

7.1 Regime III of the magnon dispersion for $R_2Ir_2O_7$……..…72

7.2 Laser dependence of the M_1 and M_2 peaks……....73

7.3 Magnetic point group analysis for AIAO pyrochlore iridate $Y_2Ir_2O_7$……74

8 Publication List …… 77

9 Korean Abstract …… 80

List of figures

Figure 1. Optical conductivity spectra $\sigma_1(\omega)$ of $Y_2Ir_2O_7$. a Optical conductivity spectra were measured at various *T* values from 10 K to 300 K (shown in the top figure). b-g We used data obtained at several T values to fit the experimental data (open circles) to the total model (red solid lines), which featured a Fano-Lorentz lineshape (colored dashed lines), ω-linear absorption (shaded region), and a very small constant background.

Figure 2. Phonon eigenmodes and the atomic displacements of $Y_2Ir_2O_7$. a-g Each Ir atom (green) is surrounded by trigonally-compressed cages formed by oxygen ions O(1) (red) and oxygen ions O(2) (orange) bonded to a Y ions (blue). Black arrows show the atomic displacement of each phonon mode.

Figure 3. Types of oxygen displacement on the basis of the Ir-O-Ir bond. a-g The O (red) displacements (black arrows) of each phonon modes are plotted on the Ir tetrahedron. Based on the largest displacement inside the yellow circle, seven phonon eigenmodes are assigned to the three types of O displacement.

Figure 4. Sizable in-plane motion of other vibrational modes. a-c The O displacements (black arrows) of Ph2 (out-of-plane bending motion), Ph4 (out-of-plane bending motion), and Ph5 (in-plane bending motion) are shown in a to c respectively. Yellow circles indicate in-plane O ion motion. Inside the yellow circles of a and b,

the direction of displacement shows two different motion simultaneously. Contrary to this, Ph5 has pure in-plane bending motion inside the yellow circle in c.

Figure 5. All-in-all-out (AIAO) spin configurations (gray arrows), Ir-O-Ir bond of $Y_2Ir_2O_7$, and classification of phonon modes based on the O ion motion. **a** O ions (red spheres) are bonded to the nearest neighboring Ir ions (blue spheres) forming the Ir-O-Ir bond. In the AIAO magnetic order, the Ir spin-canting angle is about 109.5°. From first-principles calculations, the Ir-O-Ir bond angle θ_0 was estimated to be about 126.9°. **b** The IR-active phonons of $Y_2Ir_2O_7$ cause three types of O displacement. For the in-plane stretching mode, the O ion displacement is mostly along the x_o-axis, parallel to the Ir-Ir bond. For the out-of-plane bending mode, the O ion displacement is mostly along y_o-axis, perpendicular to the Ir-O-Ir plane. For the in-plane stretching mode, the O ion displacement is mostly along the z_o-axis in the Ir-O-Ir plane.

Figure 6. Ir-O-Ir bond angle deviations caused by oxygen motion in each direction. The Cartesian coordinates of the ion are represented by x, y, and z. Δx, Δy, and Δz are deviations of the oxygen ion from its equilibrium position. Each angle and length in the bond plane are annotated; $\alpha_{1(2)}$: Ir-Ir-O bond angle on the left (right) side, θ: Ir-O-Ir bond angle, l: Ir-O bond length.

Figure 7. Relevance of variations in the Ir-O-Ir bond angle $\Delta\theta$ to phonon renormalization $\Delta\omega_0$. For all phonon modes, $\Delta\theta$ varied in a manner similar to $\Delta\omega_0$, but Δl appeared to be not directly affected (especially in the cases of Ph4 and Ph7). To facilitate direct comparison, the values plotted in this figure are dimensionless and the

rescaled Δl is reduced by a factor of three.

Figure 8. Structure distortion of octahedra and corresponding bond angle change in the pyrochlore lattice. a Structure of the pyrochlore lattice. Four Ir ions sit at each vertex of a tetrahedron. Each site within a tetrahedral unit cell is numbered from 1 to 4. b Oxygen-mediated hopping between Ir ion sites. θ is the Ir-O-Ir bond angle ang α is the Ir-Ir-O bond angle. Without breaking global lattice symmetry, the trigonal distortion of octahedra causes oxygen ion displacement from the Ir local axes.

Figure 9. a-b Dispersions for crossing magnon band (c-MB) and noncrossing magnon band (n-MB). c Magnon band topology phase diagram for some pyrochlore iridates $R_2Ir_2O_7$ (R=Y, Tb, Eu, Sm, and Nd). We note that D/J= 0.28 in Ref. [53] is the boundary between the c-MB and n-MB topology, where the Dzyaloshinskii-Moriya interaction and the Heisenberg interaction are denoted by D and J, respectively. Red dots are parameters obtained from resonant inelastic X-ray scattering (RIXS) experiments and black diamonds are parameters from quantum chemistry calculations (QCC). For $Nd_2Ir_2O_7$ and $Tb_2Ir_2O_7$, the QCC may be less accurate because of the incorrect Ir-O-Ir angles. Therefore, the QCC parameters for $Nd_2Ir_2O_7$ and $Tb_2Ir_2O_7$ are excluded. Our Raman data (blue star) suggest $Y_2Ir_2O_7$ is in the c-MB phase, contrary to the result of the QCC.

Figure 10. a Raman spectra of polycrystalline $Y_2Ir_2O_7$ at 10 K. The frequencies of the six Raman-active phonons are calculated using density functional theory calculations (solid lines). M_1 and M_2 correspond to magnetic excitations. b Temperature

(T)-dependent Raman spectra of $Y_2Ir_2O_7$. c T-dependent Raman spectra of magnetic excitation peaks in $Y_2Ir_2O_7$. For clarity, each spectral intensity I_T at various T is subtracted by the intensity of reference spectrum I_{300} at 300 K. d T-dependence of the integrated intensity of the magnetic excitations in the range of 208 and 314 cm^{-1} (black squares) and magnetic susceptibility χ_m measured at H = 0.1 T after zero-field cooling (red circles). For integration, we subtracted the 300 K spectra from the spectra at the other temperatures and integrated them in the energy range between 208 and 314 cm^{-1}.

Figure 11. a Raman spectra of $R_2Ir_2O_7$ (R: Sm, Eu, Y) at low temperature (10 K). Using density-functional-theory calculations, we assigned the six Raman-active phonon modes located in the energy region above 300 cm^{-1}. Below 300 cm^{-1}, the Raman spectra of the three compounds commonly show two peaks that could be attributed to magnetic excitations. The peaks indicated by asterisks in the $Sm_2Ir_2O_7$ data may correspond to the crystal field splitting in Sm^{3+} ion. b-d T-dependent Raman spectra of magnetic excitation peaks (M_1 and M_2) in $R_2Ir_2O_7$. e-g Integrated intensities of M peaks (black squares) and magnetic susceptibility χ_m (red circles) of $R_2Ir_2O_7$. For integration, we subtracted the 300 K spectra from the spectra at the other temperatures and integrated them in the energy region between 208 and 314 cm^{-1}. χ_m are measured at H = 0.1 T after zero-field cooling.

Figure 12. a Magnetic excitation energy diagram for $R_2Ir_2O_7$. Black lines indicate the energies of M_1 and M_2 from our Raman experiments. The magnon bandwidths obtained from the RIXS measurements are shaded in red [54–56]. b Magnon

dispersion of $Y_2Ir_2O_7$ based on the linear spin-wave theory calculations with two Hamiltonian models in this work: Model A, where J = 38.2, D = 6.9 meV and nondegenerate (triangles) ≡ M_1, triply degenerate (circles) ≡ M_2 energy; and Model B, where for J = 15.1, D = 9.0 meV with triply degenerate ≡ M_1, nondegenerate ≡ M_2 energy.

Figure 13. a Magnetic-dipole excitation in spin S=1/2 state. x and y components of the magnetic field ($H^{\pm}=H^x \pm iH^y$) operator creates the magnon and the H^z operator scatters the magnon. μ is the magnetic dipole moment of spin state. b Electric-dipole excitation in pseudospin J_{eff} = 1/2 state. Analogous to the magnetic-dipole transition, electric-dipole transition can create and scatter the magnon in pseudo-spin J_{eff} = 1/2 state configuration. An external E field can induce the electric-dipole (e·r) moment and modulate the pseudospin direction. The red and yellow area indicate the up and down spin states, respectively. c Pseudospin up and down configurations. The displacement operator of the electric-dipole transition term can change the orbital angular momentum by 1. The change in the orbital angular momentum can flip the pseudospin down state to the up state.

Figure 14. Spin-phonon coupling contributions due to Heisenberg and Dzyaloshinskii-Moriya interactions. a θ-dependent J and D curves calculated using the tight-binding model using the anchoring points J = 15.1 meV, D = 9.0 meV, and θ = 128.5°. b The second derivatives of $E_J = J(\theta)\langle S_i \cdot S_j \rangle$ and $E_D = D_{ij}(\theta)\langle S_i \times S_j \rangle$.

Figure 15. a-b Ir-O-Ir bond-angle (θ) dependence of J and D obtained from tight-binding

calculations on $R_2Ir_2O_7$ (R: Sm, Eu, Y). The calculated curves of $J(\theta)$ and $D(\theta)$ agree with the J and D values in Model B for $Y_2Ir_2O_7$ but differ markedly from the J and D values in Model A. Conversely, the calculated curves agree with the J and D values in Model A for $Sm_2Ir_2O_7$ and $Eu_2Ir_2O_7$, i.e. they have n-MB topology. Our results indicate that $Y_2Ir_2O_7$ is the only candidate in the $R_2Ir_2O_7$ system to have c-MB topology.

Figure 16. Atomic displacements of Raman active phonon modes in $Y_2Ir_2O_7$

Figure 17. a T evolution of the A_{1g} phonon. b Atomic displacement of the A_{1g} phonon of $Y_2Ir_2O_7$. c T-dependence of the phonon shift (black circles) and the full width at half maximum (FWHM, black squares in inset) of the A_{1g} phonon obtained by Lorentzian fitting. Blue solid and dashed lines are the anharmonic fitting curves for the T-dependence of the phonon shift and linewidth, respectively. Thermal fluctuations of the peak shift around T_N indicate that the fitting curve for the peak shift in c is not unique, leading to a shift of the A_{1g} phonon of approximately $\Delta\omega = 2.3 \pm 0.3$ cm^{-1}. d Contour map of the phonon shift calculated for J and D values. The peak shift is indicated by color-coding. Solid and dashed lines indicate the experimental values of the peak shift and error bars: $\Delta\omega = 2.3 \pm 0.3$ cm^{-1}. Gray circles represent the calculated peak shifts corresponding to the J and D parameters of Models A and B.

Figure 18. Ir-O-Ir bond-angle (θ) dependence of J/D obtained from tight-binding calculations on $R_2Ir_2O_7$ (R: Sm, Eu, Y). Our results indicate that $Y_2Ir_2O_7$ is the only candidate in the $Y_2Ir_2O_7$ system to have c-MB topology.

Figure 19. Variation of the D'/J' ratio as a function of the D/J ratio. The black curve is the D'/J' curve and the red solid line has a value of 0.71, which is the phase boundary between regimes II ($D'/J' < 0.71$) and III ($D'/J' > 0.71$). The D'/J' curve does not exceed 0.71, implying that regime III cannot exist when the $\mathbb{A}$ term is included.

Figure 20. Raman spectra of $Y_2Ir_2O_7$ at 10 K (upper panel) and 200 K (lower panel) were measured using a 532-nm laser (green line) and a 671-nm laser (red line).

List of Tables

Table 1. Calculated and experimental phonon frequencies of $Y_2Ir_2O_7$ at 10 K.

Table 2. Comparison of the $Y_2Ir_2O_7$ spin parameters obtained via Raman scattering with and without consideration of anisotropic exchange.

Table 3. Magnetic interaction parameters for pyrochlore iridates $R_2Ir_2O_7$ (R=Y, Tb, Eu, Sm, and Nd)

Table 4. Raman tensors for the magnetic point group $m3m'$.

Abstract

In this dissertation, we investigate the emergent phenomena on the noncollinear magnetic ordering or pyrochlore iridates. Combining the frustrated pyrochlore lattice and strong spin-orbit coupling (SOC), pyrochlore iridate system shows the exotic noncollinear magnetic ordering, so-called all-in-all-out (AIAO) magnetism. Based on this exotic magnetism, the unconventional spin-phonon coupling and nontrivial topological magnon phase emerge on the pyrochlore iridate system. Using the optical spectroscopic technique, we reveal the mechanism of this phenomena and extend our understandings of the physics of 5*d* transition metal oxide system.

For the iridium oxides, Strong SOC with comparable Coulomb interaction (U) induce the relativistic Mott insulating state, J_{eff}=1/2 state. In general, most iridate materials with their Mott state has the collinear magnetism since their square lattice structure. Different from the square lattice structure, however, pyrochlore lattice structure interrupts their long range collinear magnetic ordering and induce the magnetic frustration such as the honeycomb lattice structure. Because of strong SOC, anisotropic exchange interactions are enhanced between their magnetic ions. These interactions play an important role to stabilize the magnetic frustration and induce the noncollinear AIAO magnetism. These kind of exchange interactions are highly mediated by intermediate O ions between the nearest neighbor Ir ions. In conclusion, That's the reason why the phonon modes with O ion vibration are coupled with the spin structure. Based on this aspect, it is necessary to investigate the unrevealed coupling phenomena in 5*d* TMOs.

First, we discuss the unconventional spin-phonon coupling via Dzyaloshinskii-Moriya (DM) interaction in $Y_2Ir_2O_7$. In 3*d* TMOs, Heisenberg exchange interaction is the main contributor of spin-phonon coupling behavior. Because of the weak SOC, anisotropic exchange interactions mediated by SOC are highly suppressed. In 5*d* TMOs, however, strong SOC enhances the anisotropic exchange interactions, which are expected to be comparable to the Heisenberg exchange interactions. We find the unconventional phonon renormalization phenomena in $Y_2Ir_2O_7$ from the optical phonon spectra measured by Fourier transform infrared (FTIR) spectroscopic technique. Based on the density functional theory (DFT) calculations, we find that phonon renormalization originates from the modulation of magnetic exchange interaction via the Ir-O-Ir bending motion. Using the tight-binding model analysis, we confirm that DM interaction is the main contributor of the phonon renormalization in $Y_2Ir_2O_7$. This result suggests that strong SOC has an important role in spin-phonon coupling in 5*d* TMOs and noncollinear magnetic materials.

Second, we show the topological magnon state in pyrochlore iridates and topological phase transition between them. The ratio between DM interaction and Heisenberg interactions determined the magnon topology in pyrochlore iridate system. Because of experimental difficulties to measure magnetic signal of Ir ion, it is hard to confirm the topological magnon phase between the pyrochlore iridates. Using the Raman spectroscopy, we measured the magnetic excitation signals of pyrochlore iridates $R_2Ir_2O_7$ (*R*: Y, Eu, Sm) with high resolution. According to the previous Resonant x-ray inelastic scattering (RIXS) studies for $Eu_2Ir_2O_7$ and $Sm_2Ir_2O_7$, these signals originate from single-magnon excitations. For $Y_2Ir_2O_7$, there are two possible spin Hamiltonian models to describe the single-magnon scattering

phenomena. Using the tight-binding model analysis, we confirm the right spin Hamiltonian model parameters for $Y_2Ir_2O_7$. From this result, we find that $Y_2Ir_2O_7$ has different nontrivial magnon topology with the topology of other pyrochlore iridates. Our result strongly suggests that pyrochlore iridate system is a good platform to design the magnon topology and our result enriches the phase diagram of magnon topology.

In addition, we introduce the possible mechanism of single-magnon scattering process in J_{eff}=1/2 pyrochlore iridates. Strong SOC makes the spin-orbital entangled pseudospin states. Because of the orbital angular momentum part of pseudospin states, it is possible to scatter the magnon via electric-dipole transition. Here, we show the single-magnon scattering mechanism and their Raman tensor symmetries in pyrochlore iridate system. Our result extends the sight for the single-magnon scattering behavior in 4*d*/5*d* pseudospin materials and their enhanced intensities in Raman spectra.

Keywords: Correlated topological phases, electronic structures, Weyl semimetal, pyrochlore iridate.

Student number: 2015-20332

Chapter 1

Introduction

In this chapter, we discuss the background information on the electronic and magnetic structure of 5*d* pyrochlore iridate. We introduce the strong spin-orbit coupling and accompanying exotic ground states of iridate system, noncollinear magnetic ordering of pyrochlore iridates, and correlated topologies. In the end of this chapter, we summarize the outline of thesis on optical spectroscopic technique for this pyrochlore iridate system.

1.1 Iridate and J_{eff}=1/2 state

In the transition metal oxide (TMO) system, oxygen ion plays an important role in the electronic ground states. Oxygen ions around the transition metal ion form an octahedral structure on the TMO system. Nearest neighboring oxygen ions apply the electric field and split the degeneracy of the valence band on the transition metal ion. The *d* orbital states, valence states of transition metal ion, are split into the t_{2g} and e_g states. For e_g states, their orbital extends toward the oxygen ions, which repulse the electron. These repulsive interactions with the orbital electrons make the e_g state unstable. For t_{2g} states, however, their orbital directions are separated from the oxygen ions. Compared to e_g states, t_{2g} states are stabilized and the energy of t_{2g} states is lower than that of e_g states. In general, e_g states are separated from the t_{2g} states by 10Dq.

Electron correlations (*U*) and spin-orbit coupling (SOC) enrich the novel physics of the TMO system. Coulomb interactions between valence band electrons have an important role in emerging phenomena independent from the crystal field effect. Orbital hybridization and electron localizing effect induce the electron-electron repulsion and corresponding strong electron correlation effects. For this reason, the motion of itinerant electrons is blocked on their ions. These correlation effects make the degenerated states split and we call these materials a Mott insulator. For 5*d* TMO, the electron correlation effect is weaker than that of 3*d* TMO since the extended 5*d* orbital size. Iridates, which have 5 electrons in the 5*d* orbitals consist of the valence states, are seems to be metal. Because of the strong SOC in 5*d* materials, however, degenerated t_{2g} states are split into effective total angular

momentum states half-filled J_{eff}=1/2 doublet and fully occupied J_{eff}=3/2 quadruplet states. Combined with electron correlation, J_{eff}=1/2 doublet states become an insulator, so-called relativistic Mott states [1].

1.2 Pyrochlore iridates with All-in-all-out magnetism

In 3*d* TMO, Heisenberg exchange interactions is the dominant interactions in the spin Hamiltonian. Because of weak SOC effect in 3*d* TMO, anisotropic exchange interactions are negligible to the Heisenberg interactions. It shows different phenomena between the different type of lattice structure. First, in square lattice structure, Heisenberg interactions induce the collinear magnetic ordering between the nearest neighbor ions. Very weak anisotropic interaction makes the small amount of canting angle, but the long-range magnetic ordering still be stable. Second, in triangular (hexagonal) lattice structure, Heisenberg interaction is insufficient to stabilize the long-range magnetic ordering. As a result, magnetic frustration occurs on their lattice structure. In 5*d* TMO, however, strong anisotropic exchange interactions due to the SOC effect is comparable to the Heisenberg interactions.

Strong SOC effect has an important role in stabilization of non-collinear magnetic ordering. For example, pyrochlore lattice consist of the corner-sharing tetrahedral structure of the magnetic ions. For pyrochlore lattice structure, so-called 3*d* kagome lattice, consist of the combination of hexagonal and triangular lattice structure layer. In this lattice structure, strong SOC induce the exotic non-collinear magnetic ordering, antiferromagnetic

states with local spins pointing inside or outside the center of the tetrahedron. We called it as All-in-all-out (AIAO) magnetic ordering. This non-collinear magnetic ordering emerges on the 5*d* pyrochlore oxides, such as $Cd_2Os_2O_7$ and $R_2Ir_2O_7$, each magnetism is stabilized by the single-ion anisotropy and Dzyaloshinskii-Moriya (DM) interaction, give rise to the strong SOC.

1.3 Topology in pyrochlore iridates

Recently, the topological properties of the fermionic semimetallic systems have attracted much attention in contemporary condensed matter physics [2,3]. While some materials with both inversion and time-reversal symmetries host Dirac fermions, breaking of either of the symmetries will lead to a Weyl semimetallic phase [4]. The latter can be realized in a system with electronic correlations and strong spin-orbit coupling. For instance, pyrochlore iridate $R_2Ir_2O_7$ is among the candidate materials with topological Weyl semimetal states [5]. The noncollinear AIAO magnetism can break the time-reversal symmetry while maintaining the crystalline inversion symmetry [6].

With the above conditions, pyrochlore iridate system shows the characteristic band structure. Based on these symmetry conditions and valence J_{eff}=1/2 state, we can describe the band structure as a simple tight-binding model.

$$H_0 = \sum_{\langle i,j \rangle} c_i^{\dagger} \left(t_1 + i t_2 \boldsymbol{d}_{ij} \cdot \boldsymbol{\sigma} \right) c_j \tag{1}$$

where $c^{\dagger}$ and c indicate the fermion creation and annihilation operators, t_1 and t_2 are

spin independent and dependent hopping integrals. d and σ mean the vector of spin direction and corresponding operators between the nearest neighbor tetrahedron site i and j. From the previous theoretical studies with tight-binding model calculations, they suggest the characteristics of nontrivial topological band structure using the diagonalized effective Hamiltonian.

$$H_D = E_0\mathbb{I} + \boldsymbol{v}_0 \cdot \boldsymbol{q}\mathbb{I} + \sum_{l=1}^{3} \boldsymbol{v}_l \cdot \boldsymbol{d}\sigma_l \tag{2}$$

where I and σ indicate identity and Pauli matrix operators for electronic eigenstates, v_0 and v_l are velocity vectors. And $\boldsymbol{q}=\boldsymbol{k}-\boldsymbol{k}_0$; $\boldsymbol{k}_0$ is the topological nontrivial k point in the brillouin zone (BZ). Near the topological nontrivial points, band structure shows the linear dispersion for any directions. Based on this characteristics of topological materials, numerous emergent phenomena of $R_2Ir_2O_7$ have been discussed extensively in the literature, such as metal to insulator transition [7], anomalous Hall effect [8], and topologically nontrivial Weyl semimetal phase [5,9].

1.4 Outline of Thesis

In this thesis, we investigate the underlying physics emerging between the various degrees of freedom using the optical spectroscopic technique. In Chapter 1, we introduce the novel state of 5*d* iridate system, non-collinear magnetic ordering, and corresponding topological issues of this material system. In Chapter 2, we explain the experimental techniques for measuring the optical spectra. In Chapter 3, we describe the unconventional spin-

phonon coupling via DM interaction. Using the phonon spectra analysis, we suggest the evidence of this new mechanism. Chapter 4, we show the rich phase of topological magnon phase diagram and suggest the evidence of nontrivial topological magnonic material $Y_2Ir_2O_7$. Also, we provide the new mechanism for single-magnon scattering process. This mechanism can be applied to the pseudospin materials explaining the magnetic excitation peaks of their Raman spectra.

Chapter 2

Experimental Methods

For a long time, visible light has mediated the human and materials. From the sunlight, people could have distinguished the various material properties, such as the position, status, and even shape of it. After invention of optical equipment, our sight for the materials were extended from the small particle scale to the far universe scale. As a theoretical aspect, also, speed of light became a reference of electrodynamics and relativistic theory to the physics society in 20th century.

Nowadays, invisible light provides the insight of the material properties. Using the Infrared spectra, we can obtain the information of transport properties, resonance frequencies of lattice vibrations, and band gap size for describing the electronic band structure, quantitively. Fortunately, this measurement technique is nondestructive.

In this chapter, we introduce the experimental techniques to obtain the optical spectra of materials. Using the Fourier Transform Infrared spectroscopy and spectroscopic ellipsometry, we obtain the IR-active phonon spectra. In addition, we obtain the Raman-active phonon spectra and magnon scattering signal using Raman spectroscopy. Based on the understandings of the spectroscopy technique, we can investigate the underlying physics.

2.1 Introduction to optical spectroscopy

In this section, we introduce the measurement techniques of optical spectroscopy. For a long time, optical spectroscopy has played an important role in revealing the physical feature of materials. Using the optical spectroscopic measurement, we can obtain the reflectance and transmission of the materials. Based on this information, we can investigate the various features from physical properties. In the transition metal oxide system, Coulomb interaction between electrons induce the coupling phenomena of various degrees of freedom. Using the optical spectroscopic measurement, we can obtain the various physical excitation phenomena simultaneously which can help us understanding the coupling phenomena such as phonon (collective excitation of lattice vibration) and magnon (collective excitation of spin fluctuation).

2.2 Spectroscopic ellipsometry

This section introduces the details of spectroscopic ellipses with cryogenic greenhouses. Powerful tools are sensitive to very thin layers of material (~nm). Elliptical measurement techniques measure the polarization dependence of reflective light, i.e., we illuminate polarized light and obtain reflective light. Here you can see the intensity ratio and polarization rotation angle between the two lights. The high sensitivity of the ellipsoid comes from this magnetic reference property. The actual and virtual parts of the dielectric constant can be

obtained directly from two independent experimental variables, variables (intensity ratio Tan(Ψ) & polarization rotation difference Δ). It is easy to convert complex dielectric constants into complex photoconductors. In this regard, spectroscopic ellipses are a perfect tool because they do not require Kramers-Kronig analysis and have very high sensitivity.

2.3 Fourier transform infrared spectroscopy

Fourier Transform infrared spectroscopy (FTIR) can be used to make energy range reflective measurements on reflective geometry equipped with cryogenic chambers and internal gold evaporation ports. Compared to other spectroscopy tools, FTIR can measure the intensity of all frequencies at the same time. This reduces measurement time and enables high frequency/energy resolution, increasing the accuracy of the experiment. The FTIR consists of a beam splitter, a fixed mirror and a moving mirror.

The basic geometry of FTIR is the same as that of the Michelson interferometer. If the distance from the beam-splitter to the fixed mirror and the moving mirror is equal, the phase of the two beam paths is consistent, resulting in constructive interference. In this case, the detector has the highest intensity. When the moving mirror changes position and the beam path difference is λ/4, the phase becomes 180°, resulting in destructive interference. As the number of frequencies increases, the detector obtains overlapping of various isotopic waveforms to generate an intervention degree. When the path difference is zero, all frequencies have maximum intensity and produce the signal with the greatest overlap. After generating a consistency chart, it touches the sample, reflects, or transmits according to the shape of

the sample. When absorbed from the sample, the interferometer is modified. Finally, the interferogram is converted into an intensity spectrum in terms of light frequency. Considering the light absorption and cryogenic windows of the beam splitter, the obtained reflective spectra are not absolute. Therefore, we change the position of the sample for reference measurement during the measurement. The gold mirror is typically used as a reference (indicating the intensity corresponding to reflection 1). Reflectivity is obtained after dividing the intensity spectrum of the sample by the intensity spectrum of the gold mirror. However, this is only true if the surface area of the sample and the gold mirror is exactly the same. In most cases, the size and shape of the sample are different from that of the gold mirror. To compensate for the difference in surface area between the sample and the reference, the gold on the sample surface evaporates in the field and the alignment conditions remain the same. The measurement is repeated after the sample is coated with gold, and the gold-plated sample is split into a gold mirror to obtain surface information for the sample. Finally, the former is divided into the latter to obtain an absolute reflectivity. *in-situ* gold evaporation techniques also correct against misalignment of optical units, time variations in beam intensity, and rough surfaces of samples.

Heat energy in most materials changes physical properties with temperature. In addition, changing the temperature is a good way to control magnetic order or structural transitions. Use a cold finger and heater-equipped Ultra High Vacuum (UHV) chamber to adjust the temperature of the sample. Keep the angle of entry close to 0 (~7 deg) while attaching a polypropylene window to allow the light source to enter. A minimum temperature of 10K to 450 K can be controlled using liquid He or liquid nitrogen. The temperature sensor uses

silicon diodes which can be damaged at temperatures above 500K. UHV chamber is needed because of ice. The formation of the sample can give a large signal to the experimental value. Bake the chamber and keep the pressure below 10^{-8} mbar to minimize the ice signal.

2.4 Raman spectroscopy

The Raman spectroscopic measurement is collecting the scattering light from the sample. Different from the reflectivity measurement, the Raman scattering process is related to the inelastic transition process.

The scattering process consists of two types; one is an elastic process and the other is an inelastic process. Incident light from the light source excites the ground-state electron to the virtual state. Since the virtual state is unstable, this state emits its energy by scattering photon. For the elastic scattering process, emission energy from the virtual state is the same as the energy of incident light. It is called Rayleigh scattering. In general, Rayleigh scattering has no information, because of the same energy of incident and scattered light from the virtual state.

However, it is possible to obtain the difference between the energy of incident and scattered light. Inelastic scattering, so-called the Raman scattering, process shows different responses depending on the energy differences of the incident and scattered light. Because of the mediating particles, which obtain the energy from the virtual state, the Raman process leaves the excited state of mediating particles, such as phonon or magnon.

At the first time, it was hard to measure the scattering light using the visible ray from

the daylight. Because the ratio of scattering light from the incident light is 10^{-9}. However, we overcame this problem using the laser technique and microscopy. Using the laser and microscope, the incident light could be focused on the small spot of the sample with a high intensity of light. Through the enhanced intensity of light, we can collect a lot of photons from the sample. Also, the small size of the beam spot distinguishes the few μm-size domains of a polycrystal, such as the impurities or rough surfaces. Focusing on the right domain, we can get clear spectral data of the pure samples.

Chapter 3

Result and Discussion I:

IR spectroscopy

In this chapter, we suggest the unconventional spin-phonon coupling mechanism in $Y_2Ir_2O_7$. Spin-phonon coupling (SPC) plays a critical role in numerous intriguing phenomena of TMOs. In *3d* and 4*d* TMOs, the coupling between spin and lattice degrees of freedom is known to originate from the exchange interaction. On the other hand, the origin of SPC in 5*d* TMOs remains to be elucidated. To address this issue, we measured the phonon spectra of the 5*d* pyrochlore iridate $Y_2Ir_2O_7$ using optical spectroscopy. Three infrared-active phonons soften below the Néel temperature of $T_N \approx 170$ K, indicating the existence of strong SPC. Simulations using density functional theory showed that the coupling is closely related to the Ir-O-Ir bond angle. A tight-binding model analysis reveals that this SPC is mainly mediated by the DM interaction rather than the usual exchange interaction. We suggest that such unconventional SPC may be realized in other 5*d* TMOs with non-collinear magnetic order.

3.1 Introduction

3.1.1 Brief history of optical studies in 5*d* pyrochlore materials

Combined with J_{eff}=1/2 states and electron correlation U, 5*d* pyrochlore oxides are the fascinating platforms to study optical spectroscopy. Relative Mott insulating states of 5*d* pyrochlore iridates and DM interactions stabilize the non-collinear AIAO magnetic ordering in this cubic system. Since the AIAO magnetic ordering protects the cubic symmetry, Weyl semimetallic state can be expected to emerge. Previous optical spectroscopic studies suggested the candidate materials show the linear optical response, which is the signature of the Weyl semimetallic states.

3.1.2 Spin-phonon coupling in 5d TMO

In general, we can describe the physics of most spin-related phenomena in solids using the spin Hamiltonian (H_{spin}). This can be written as a sum of the isotropic exchange (IE) interaction, the Dzyaloshinskii-Moriya (DM) interaction, the anisotropic exchange (AE) interaction, and the single-ion anisotropy (SIA) [10–12]:

$$H_{\text{spin}} = \sum_{ij}^{nn}\left[J_{IE}\left(\mathbf{S}_i \cdot \mathbf{S}_j\right) + \mathbf{D}_{ij} \cdot \left(\mathbf{S}_i \times \mathbf{S}_j\right) + \mathbf{S}_i \cdot \mathbf{\Gamma}_{ij} \cdot \mathbf{S}_j\right] + A\sum_i(\mathbf{n}_i \cdot \mathbf{S}_i)^2. \quad (3)$$

J_{IE}, D_{ij}, and Γij are the coefficients of the IE, DM, and AE interactions, respectively. A and n_i are the coefficient of the SIA and the direction vector of corresponding easy-axis. S_i and S_j are the spins at the nearest neighboring i^{th} and j^{th} sites [13,14]. Spin interactions are mediated by the Coulomb interaction of electrons at neighboring sites and are highly

dependent on the positions of the neighboring ions [15]. Consequently, J_{IE}, D_{ij}, Γ_{ij} and/or A terms can be dynamically modulated by a lattice vibration, resulting in SPC and a renormalization of the phonon frequencies.

A large number of studies have focused on 3*d* and 4*d* TMOs where the SPC may be explained in terms of dynamic modulation of the IE interaction. $RMnO_3$ (*R*: rare-earth site ion) [16–27], one of the widely investigated 3*d* TMOs, shows strong SPC phenomena which is closely linked with multiferroicity [16,17,20–23,28]. Geometrically frustrated TMOs are also known to have strong SPC [18,19,25,26]. For example, in 3*d* ACr_2O_4 (*A*: Cd, Zn), the coupling leads to spin-driven Jahn-Teller effects which relieve the magnetic frustration [25–27]. Similarly, strong SPC could occur also in 4*d* $Y_2Ru_2O_7$ and $Y_2Mo_2O_7$ with spin-glass state [18,19]. All of these SPC phenomena have been well explained by the dynamic modulation of the IE interaction [16–27].

The H_{spin} in equation (1) indicates that other magnetic interactions could also induce SPC, but such possibilities have not been investigated to date. Recently, the DM interaction has attracted significant attention due to its critical role in multiferroics and topological materials [5,29,30]. It is therefore highly desirable to explore the possibility of novel SPC mediated via the DM interaction. Equation (3) shows that such an alternative mechanism requires that both D_{ij} and $\langle S_i \times S_j \rangle$ be large. It should be noted that the DM interaction term originates from spin-orbit coupling (SOC) [13]. The SOC is the relativistic interaction that increases roughly with Z^2 (*Z*: atomic number) [31]. For example, the SOC of 5*d* TMOs is about 500 meV, much larger than that of 3_d TMOs (typically < 10 meV). Therefore, compounds containing heavy elements are better candidates to search for unconventional SPC

based on strong SOC.

Among 5*d* TMOs, pyrochlore iridates are good candidates to search for new types of SPC. First, they have an intriguing ground state, called J_{eff} =1/2 state [1,14], due to strong SOC. Second, pyrochlore iridates host an intriguing form of antiferromagnetism, namely the AIAO magnetic order [5,32]. All spins of one (neighboring) tetrahedron point inward (outward) [33]. This non-collinear spin configuration results in a large $\langle \mathbf{S}_i \times \mathbf{S}_j \rangle$ value in equation (3). Significant dynamic modulation of the DM interaction can therefore lead to a renormalization of the phonon frequencies which cannot be fully explained by the IE interaction alone

3.2 Experimental details

We obtained a high-quality polycrystalline $Y_2Ir_2O_7$ sample using Y_2O_3 (99.999%; Alfa Aesar) and IrO_2 (99.9%; Sigma Aldrich) powders. As IrO_2 evaporates easily during sintering, we used 4–10% more IrO_2 than suggested by the stoichiometric ratio, Y_2O_3: IrO_2 = 1:2. The mixture was pelletized and calcinated in a box furnace at 760°C for 48 hours. After re-grinding and re-pelletizing, several annealing cycles were performed at temperatures between 900°C and 1030°C, each for 48 hours. High-density targets were prepared for optical experiments by pelletizing $Y_2Ir_2O_7$ powder using a high-pressure anvil (NCAP-035; Nanki Engineering) operating at 4.3 GPa. Samples with densities > 87% were polished to render the surfaces shiny and flat.

X-ray diffraction (XRD) was used to verify the quality of our $Y_2Ir_2O_7$ crystals, as outlined below. Powder XRD data were obtained using a high-resolution powder diffractometer (D8 Discover; Bruker) operating at wavelengths of 1.54590 and 1.544310 Å ($K_{\alpha 1}$ and $K_{\alpha 2}$, respectively).

We measured the near-normal reflectance spectra R(ω) by Fourier transform infrared spectroscopy (VERTEX 80v; Bruker) and spectroscopic ellipsometry (V-VASE; J.A. Woollam). To compensate for the effects of rough surface, we normalized R(ω) relative to those measured after in-situ gold evaporation [34]. From R(ω), we calculated the optical conductivity spectra, $\tilde{\sigma}(\omega) = \sigma_1(\omega) + i\sigma_2(\omega)$ using the Kramers-Kronig transformation. To track the spectral components, we fitted $\sigma_1(\omega)$ to a Fano-Lorentz line shape, given by

$$\sigma_1(\omega) = \frac{\mathrm{SW}}{4\pi\Gamma}\frac{q^2+2q\epsilon-1}{q^2(1+\epsilon^2)}, \tag{4}$$

where ω is the angular frequency of the photon, $\epsilon = (\omega - \omega_0)/\Gamma$ is a dimensionless parameter for reduced energy, and q is the Fano asymmetry parameter. Here, ω_0, Γ, and $\mathrm{SW} = 8\int \sigma_1(\omega')d\omega'$ are the resonance frequency, linewidth, and spectral weight of the phonon, respectively.

3.3 Spectroscopic investigation

3.3.1 Optical phonon spectral results

We investigated the IR-active phonons of a $Y_2Ir_2O_7$ polycrystalline sample. The photon energy range was $6 \leq \hbar\omega \leq 5{,}000$ meV and T ranged from 10 to 300 K. The $\sigma_1(\omega)$ spectra

show seven IR-active phonons in $Y_2Ir_2O_7$ below 90 meV [35,36], as expected for the pyrochlore structure [36,37]. The experimental $\sigma_1(\omega)$ spectra also showed several weak peaks, possibly due to impurities [38], but they did not influence our phonon analysis of $Y_2Ir_2O_7$. For later discussion, we label the seven strong phonon modes as Ph1 to Ph7 in order of increasing frequency, ω.

Three of the IR-active phonons exhibit an anomalous *T*-dependence. The *T*-dependent evolution of each phonon are presented. The blue arrows show that Ph1, Ph2, Ph3, and Ph7 blueshift (i.e., harden) monotonically with decreasing *T*. On the other hand, the red arrows indicate that Ph4, Ph5, and Ph6 redshift (i.e., soften) abruptly.

3.3.2 Lorentzian fitting

To perform a more quantitative analysis, we fitted the $\sigma_1(\omega)$ spectra with a Fano-Lorentz model. We carefully fitted our experimental data to a phenomenological model that included the Fano-Lorentz model, ω-linear absorption, and a constant background. The following optical conductivity model was used:

$$\sigma_1(\omega) = \frac{\mathrm{SW}}{4\pi\Gamma}\frac{q^2+2q\epsilon-1}{q^2(1+\epsilon^2)} + y_0\cdot\omega + y_1, \tag{5}$$

where y_0 and y_1 are constants, ω the angular frequency of the photon, $\epsilon = (\omega - \omega_0)/\Gamma$ a dimensionless parameter termed reduced energy, SW the spectral weight, Γ the linewidth, *q* the Fano asymmetry parameter, and ω0 the resonant frequency of the phonon.

We present the full range ($6 \leq \omega \leq 100$ meV) of the IR-active phonon spectra over the

entire T band employed. We obtained IR spectra from 10 K ≤ T ≤ 300 K (totally 11 temperature points). We show the plots of the experimental data (open circles) along the individual fitting curves for Ph4, Ph6, and Ph7 at the representative temperatures T = 10 K and 300 K. Y_2O_3 impurity peaks (black dashed-dotted lines) were also considered. Ph6 was clearly isolated from the spectral overlap. No significant interference was noted, although the spectral weight of Ph6 was close to two phonon peaks (Ph5 and Ph7 energy) and thus

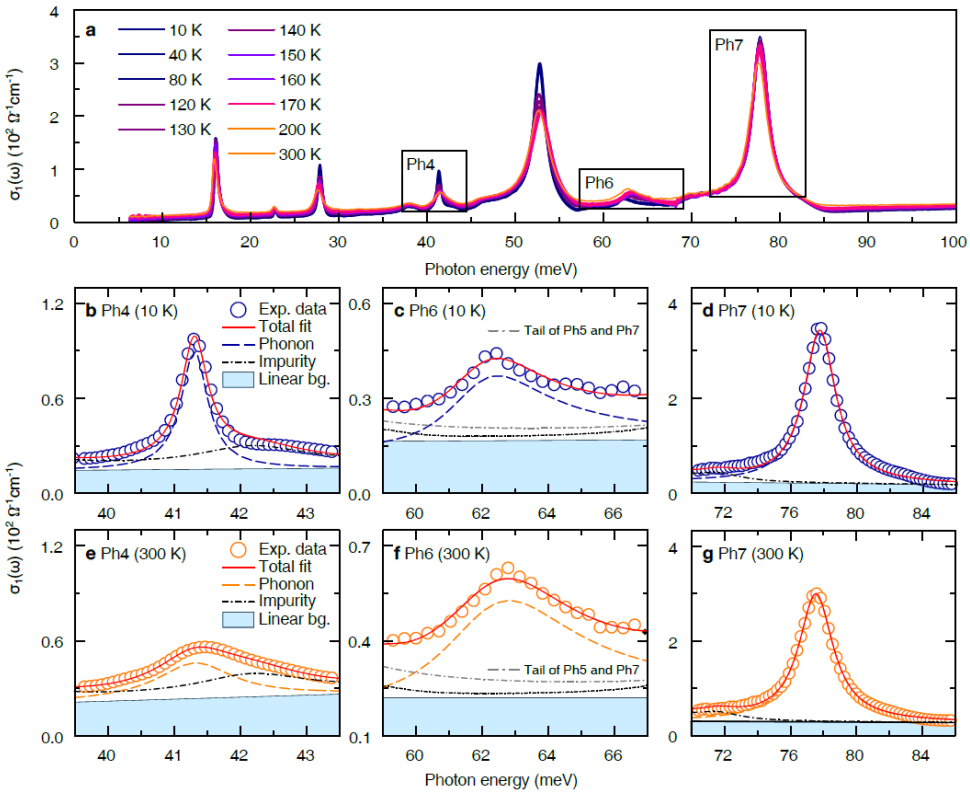

Figure 1. Optical conductivity spectra $\sigma_1(\omega)$ of $Y_2Ir_2O_7$. a Optical conductivity spectra were measured at various T values from 10 K to 300 K (shown in the top figure). b-g We used data obtained at several T values to fit the experimental data (open circles) to the total model (red solid lines), which featured a Fano-Lorentz line-shape (colored dashed lines), ω-linear absorption (shaded region), and a very small constant background.

unavoidably overlapped with their tails, the sums of which were also plotted (gray dashed-dotted lines).

We employed the Fano model to fit asymmetric line-shapes for Ph1 and Ph6, while we used symmetric Lorentz model for the other phonons. Here, the slightly asymmetric line-shape is probably due to interference between continuum, the electron-phonon coupling. But their small asymmetry level means the electron-phonon coupling is weak so that it doesn't affect so much to the phonon parameters. Importantly, we found that values of the asymmetry parameter q are nearly constant across T_N, which suggests that the electron-phonon coupling may be irrelevant to the observed anomalous phonon shifts. The Néel temperature, T_N (red dashed line), is approximately 170 K.

A comparison with the phonon-phonon scattering theory can provide an insight into the phonon renormalization of $Y_2Ir_2O_7$. The red lines indicate the theoretical phonon frequencies, ω0th, expected based on the simple phonon-phonon scattering theory [38,39]. The $\omega_0(T)$ of Ph7 is well-described by the theory. On the other hand, the $\omega_0(T)$ of Ph4, Ph5, and Ph6 show abrupt redshifts at $T_N \approx 170$ K that are not captured by the theory. For later discussion, we define the frequency difference, $\Delta\omega_0(T) \equiv \omega_0^{th}(T) - \omega_0(T)$ at $T = 10$ K. In addition, the $\Gamma(T)$ of Ph4, Ph5, and Ph6 also show kink-like features near T_N. The phonon linewidth, the inverse of the lifetime, can become smaller in the ordered state which is away from the phase transition. However, earlier XRD and neutron diffraction experiments showed that AIAO magnetic ordering in pyrochlore iridates is not accompanied by a structural transition [40–42]. Therefore, we can conclude that the anomalous T-dependence of Ph4, Ph5, and Ph6 should be coupled to the AIAO magnetic order.

3.4 Theoretical calculation

3.4.1 DFT calculations

To obtain the phonon eigenmodes of $Y_2Ir_2O_7$, we performed DFT + U calculations with the PBEsol exchange correlation function implemented in VASP [43]. We chose the effective U = 1.5 eV to simulate the local Hubbard interaction of Ir [32], and used the non-collinear DFT formalism to express the AIAO magnetic configuration. We fully optimized the lattice structure and obtained Ir-O-Ir angle $\theta_0 \approx 126.9°$. We calculated the zone-center phonon modes using the frozen-phonon method.

DFT calculations were performed to determine the phonon frequencies and corresponding eigenmodes of $Y_2Ir_2O_7$. The AIAO spin configuration of the pyrochlore structure was used for the calculations. These spins are aligned along the local Ir [111] axis in the Ir tetrahedra. Spin-canting angle $\theta_{spin} = \cos^{-1}\left(-\frac{1}{3}\right) \approx 109.5°$ in the Ir-O-Ir plane, which is marked as a blue area. Here, we choose the xo- and zo-axes of the local coordinates for O ions in the Ir-O-Ir plane, and the yo-axis perpendicular to the plane. Our DFT calculations suggest that the Ir-O-Ir bond angle θ_0 is about 126.9°. This is close to the experimental values from 127.5 to 128.5° measured by neutron diffraction and XRD [40,44], respectively. The DFT-calculated phonon frequencies agree well with the experimental values and therefore support the validity of our calculations.

The DFT calculations yielded phonon eigenmodes corresponding to those of the measured IR-active phonons. All ion displacements of each vibration mode were identified. Based on the predominant ion displacements, we assigned the following individual phonon

modes.

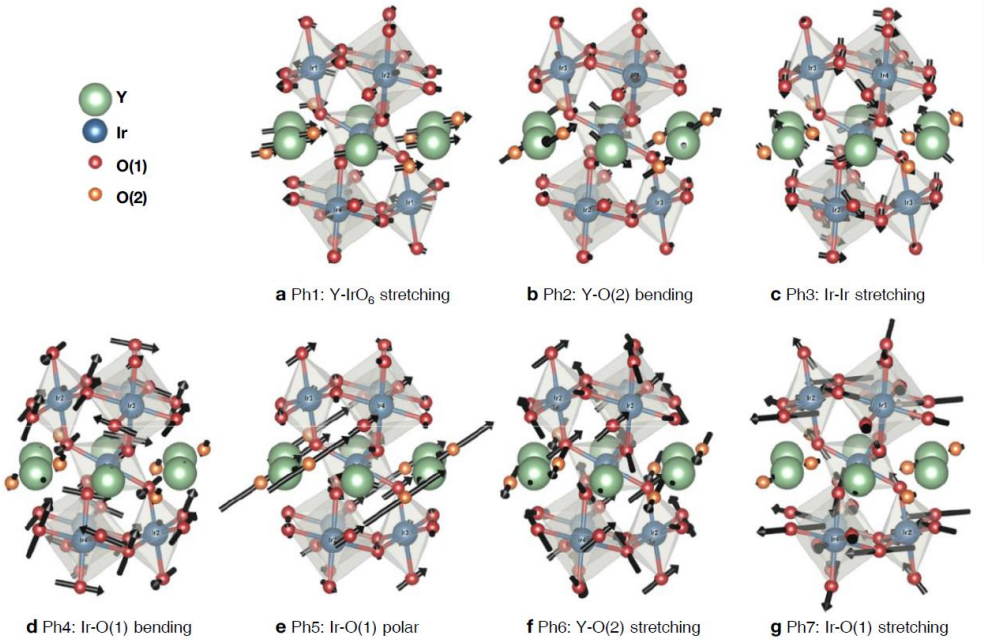

Figure 2. Phonon eigenmodes and the atomic displacements of $Y_2Ir_2O_7$. a-g Each Ir atom (green) is surrounded by trigonally-compressed cages formed by oxygen ions O(1) (red) and oxygen ions O(2) (orange) bonded to a Y ions (blue). Black arrows show the atomic displacement of each phonon mode.

To obtain further insight into the phonon renormalization, let us focus on the Ir-O-Ir bond. Note that O is the lightest element in $Y_2Ir_2O_7$, so its vibration amplitude should be largest. In this context, the motion of the O ion between the neighboring Ir spins plays an important role in the electron hopping along the Ir-O-Ir path.

The seven IR-active phonon modes can be classified into three categories based on the dominant motion of the O ions along the xo, yo, and zo-directions. We showed how to distinguish the direction of O displacement relative to the variation of Ir-O-Ir bond angle θ. By using this classification, we can assign each phonon eigenmodes to three vibrational motion. Although the IR-active phonon modes have complex vibrational motion, it is

possible to distinguish each mode by choosing the largest O displacement in the unit cell. Based on these dominant displacements, we as-signed seven phonon modes to three vibrational motion below: Stretching motion, In-plane bending motion, and Out-of-plane bending motion.

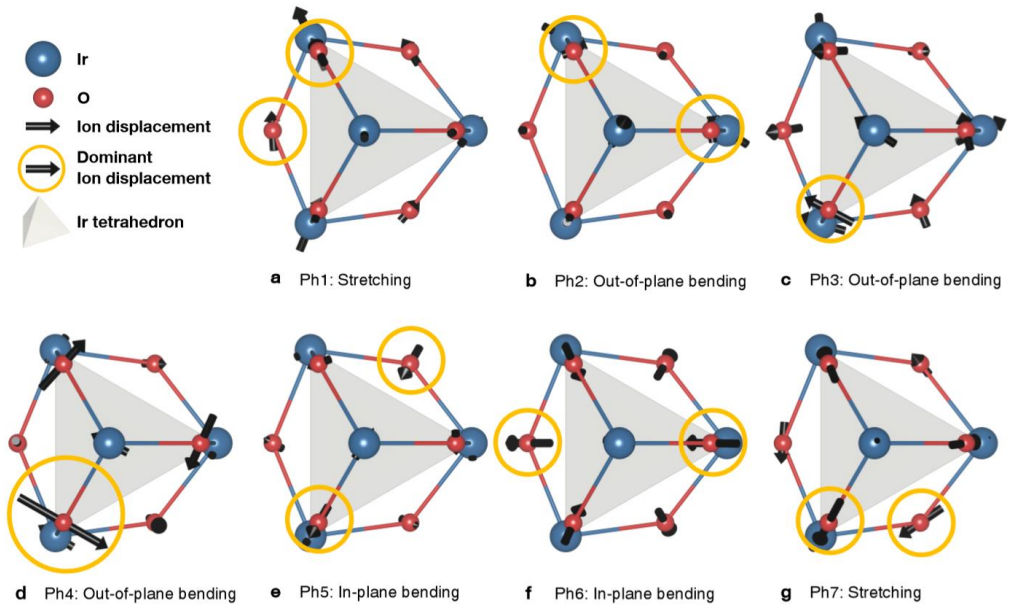

Figure 3. Types of oxygen displacement on the basis of the Ir-O-Ir bond. a-g The O (red) displacements (black arrows) of each phonon modes are plotted on the Ir tetrahedron. Based on the largest displacement inside the yellow circle, seven phonon eigenmodes are assigned to the three types of O displacement.

Oxygen displacement explains the anomalous phonon behavior because the O position is highly entangled with the Ir-O-Ir bond angle (a key parameter of our analysis). Ph2 and Ph4 induce O displacement along out-of-plane directions, with no significant effect on the bond angle θ. Although Ph4 exhibits primarily out-of-plane bending vibrations, the large displacement is accompanied by sizable in-plane displacement. For Ph5, pure in-plane motion drives the large angle deviation.

The classification is shown in Fig. 5b: Ir-O-Ir stretching (Ph1 and Ph7), out-of-plane bending (Ph2, Ph3, and Ph4), and in-plane bending (Ph5 and Ph6) motion, respectively. It should be noted that there are two kinds of O ions: one participating in the Ir-O-Ir bond and the other between Y ions.

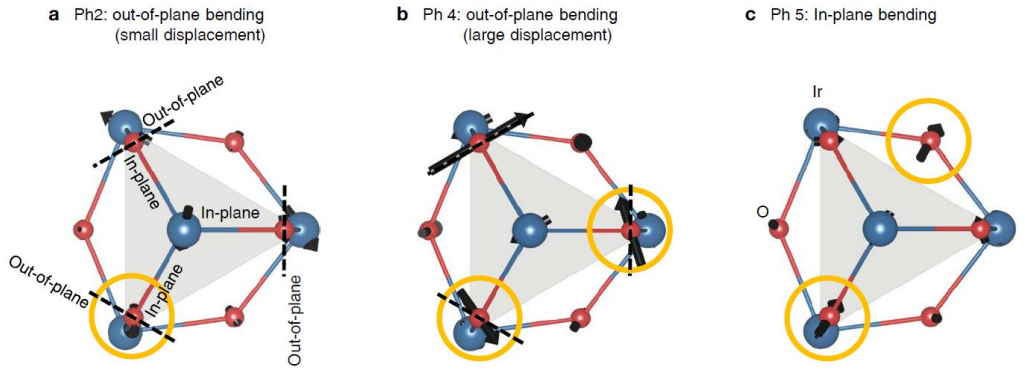

Figure 4. Sizable in-plane motion of other vibrational modes. a-c The O displacements (black arrows) of Ph2 (out-of-plane bending motion), Ph4 (out-of-plane bending motion), and Ph5 (in-plane bending motion) are shown in a to c respectively. Yel-low circles indicate in-plane O ion motion. Inside the yellow circles of a and b, the direction of displacement shows two different motion simultaneously. Contrary to this, Ph5 has pure in-plane bending motion inside the yellow circle in c.

In Ph5 and Ph6, O ions vibrate along the zo-direction, as shown in Fig. 5b. For Ph6, all of the O ions in Ir-O-Ir bond participate in the in-plane vibrational motion. However, for Ph5, only one-third of O ions in the Ir-O-Ir bond participate. It makes the difference in the average change of angle θ between two distinct eigenmodes. The magnitude of O ion displacement attributable to in-plane bending motions (Ph5 and Ph6) along the y-direction is given by Δy.

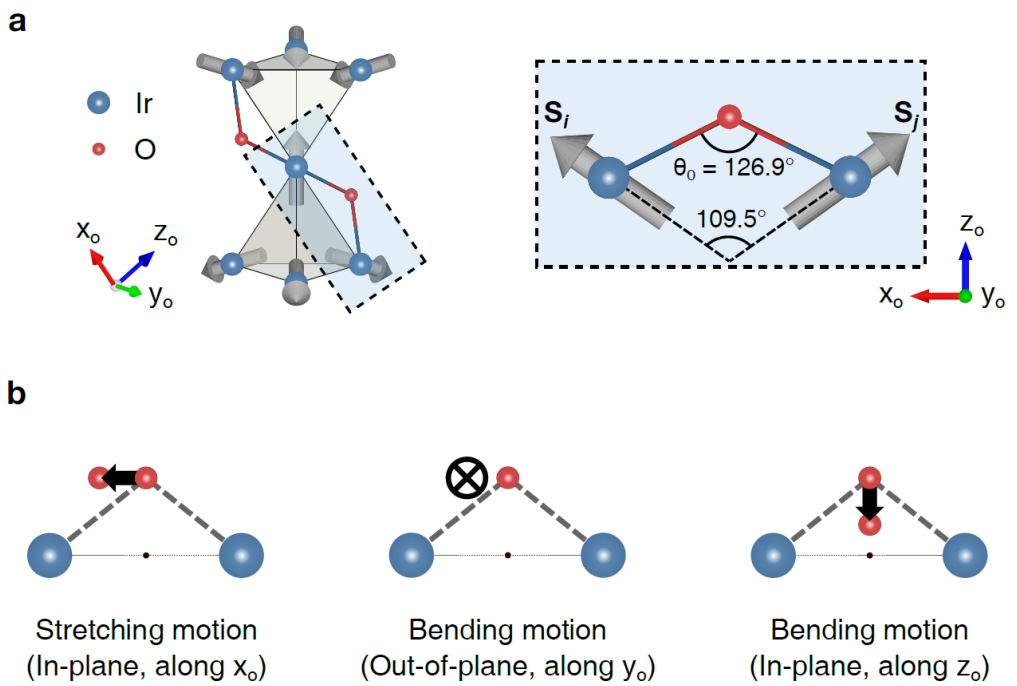

Figure 5. All-in-all-out (AIAO) spin configurations (gray arrows), Ir-O-Ir bond of $Y_2Ir_2O_7$, and classification of phonon modes based on the O ion motion. **a** O ions (red spheres) are bonded to the nearest neighboring Ir ions (blue spheres) forming the Ir-O-Ir bond. In the AIAO magnetic order, the Ir spin-canting angle is about 109.5°. From first-principles calculations, the Ir-O-Ir bond angle θ_0 was estimated to be about 126.9°. **b** The IR-active phonons of $Y_2Ir_2O_7$ cause three types of O displacement. For the in-plane stretching mode, the O ion displacement is mostly along the x_o-axis, parallel to the Ir-Ir bond. For the out-of-plane bending mode, the O ion displacement is mostly along y_o-axis, perpendicular to the Ir-O-Ir plane. For the in-plane stretching mode, the O ion displacement is mostly along the z_o-axis in the Ir-O-Ir plane.

Three parameters are corresponding Ir-O-Ir bond angle θ, Ir-O bond length l, and the Ir-Ir-O bond angle α. Using three parameters and the first-order approximation, we obtain

$$y = y - y_0 \cong \left(\frac{l}{\cos\alpha}\right)\Delta\alpha = \left(\frac{l}{\sin(\theta/2)}\right)\Delta\alpha, \tag{6}$$

when $\Delta\alpha << 1$ (where $\theta = \pi - 2\alpha$).

$$\therefore \boldsymbol{\Delta\theta} \cong -2\sin(\theta/2)\left(\frac{\boldsymbol{\Delta y}}{\boldsymbol{l}}\right). \tag{7}$$

After approximation, the angle deviation Δθ is proportional to Δy. However, the angle deviation of the other cases is proportional to $(\Delta x)^2$ and $(\Delta z)^2$.

In-plane bending motions (Ph5, Ph6) induce oxygen displacement in the positive x-direction is

$$\Delta x = \left(\frac{l}{\cos\alpha}\right)\frac{\Delta\alpha_1}{\tan\alpha \pm \Delta\alpha_{1(2)}}, \tag{8}$$

when Δα << 1. If we rearrange the equation above, we obtain

$$\Delta\alpha_{1(2)} \cong \tan\alpha\left(\frac{\Delta x}{l}\sin\alpha\right) \pm \tan\alpha\left(\frac{\Delta x}{l}\sin\alpha\right)^2, \tag{9}$$

where $\frac{\Delta x}{l}\sin\alpha \ll 1$. By comparing the two equations, we obtain

$$\therefore \boldsymbol{\Delta\theta} = \Delta\alpha_2 - \Delta\alpha_1 = -2\tan\alpha\left(\frac{\Delta x}{l}\sin\alpha\right)^2 = -\frac{2}{\tan(\theta/2)}\left(\frac{\boldsymbol{\Delta x}}{\boldsymbol{l}}\cos(\theta/2)\right)^2. \tag{10}$$

In the case of out-of-plane bending motions (Ph2, Ph3, and Ph4) where Δz induced by oxygen motion is in the positive z-direction

$$l\cos\alpha \cong (l + \Delta l)(\cos\alpha - \sin\alpha\,\Delta\alpha), \tag{11}$$

where Δα << 1. If we rearrange the equation above, we have

$$\frac{\Delta l}{l} = \frac{\tan\alpha\Delta\alpha}{1-\tan\alpha\Delta\alpha} \cong \tan\alpha\,\Delta\alpha, \tag{12}$$

when Δα << 1. According to the Pythagorean theorem

$$l + \Delta l = \sqrt{l^2 + (\Delta z)^2}. \tag{13}$$

Therefore,

$$\frac{\Delta l}{l} = \frac{\sqrt{l^2+(\Delta z)^2}-l}{l} \cong \frac{1}{2}\left(\frac{\Delta z}{l}\right)^2 \tag{14}$$

when $\frac{\Delta z}{l} \ll 1$. By comparing the two equations for Δl/l, we obtain

$$\Delta\alpha \cong \frac{1}{2\tan\alpha}\left(\frac{\Delta z}{l}\right)^2, \tag{15}$$

where $\theta = \pi - 2\alpha$. As a result,

$$\therefore \boldsymbol{\Delta\theta} \cong -\frac{\tan(\theta/2)}{2}\left(\frac{\boldsymbol{\Delta z}}{\boldsymbol{l}}\right)^2. \tag{16}$$

For the in-plane bending motion, the O displacement is parallel to the zo-direction, making the associated θ change about 100 times larger than the other motions. There are two possible contributors to phonon frequency, the Ir-O-Ir bond angle and the Ir-O-Ir bond length. For conventional SPC, the bond length is the most critical parameter for modulating the IE interaction.

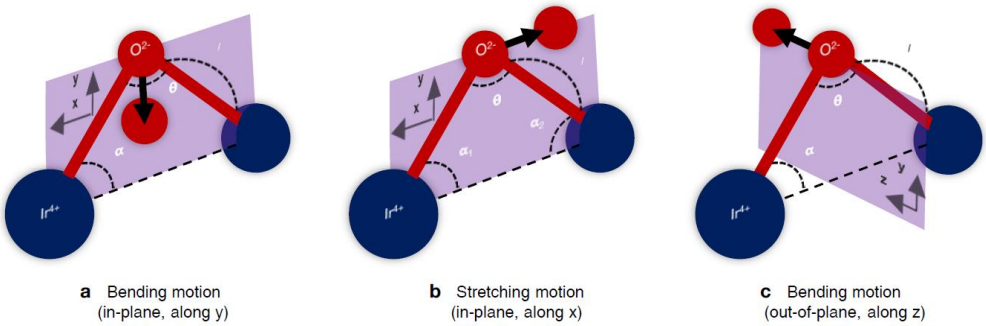

Figure 6. Ir-O-Ir bond angle deviations caused by oxygen motion in each direction. The Cartesian coordinates of the ion are represented by x, y, and z. Δx, Δy, and Δz are deviations of the oxygen ion from its equilibrium position. Each angle and length in the bond plane are annotated; $\alpha_{1(2)}$: Ir-Ir-O bond angle on the left (right) side, θ: Ir-O-Ir bond angle, l: Ir-O bond length.

Change in the bond length may affect the overlap integral significantly, resulting in a sizable change in J_{IE}. We quantitatively compared their individual contributions.

For each phonon mode, we obtained the standard deviations of changes in Ir-O-Ir bond angles and of the Ir-O lengths following 0.01 Å lattice perturbations. We assumed that the magnitude of the ionic displacements associated with each eigenmode is ~ 0.01 Å. Then,

we calculated the concomitant bond angle change, $\Delta\theta \equiv \theta - \theta_0 = \theta - 126.9°$, and bond length change, $\Delta l \equiv l - l_0$. The calculated $\Delta\theta/\theta_0$ and $\Delta l/l_0$ ratios are plotted as a bar graph. The black squares represent the measured phonon frequency deviations $\Delta\omega 0$ divided by the phonon frequencies ω_0 at T = 10 K. The white-outlined and blue-filled rectangles indicate the angle changes $\Delta\theta/\theta_0$ and the length changes $\Delta l/l_0$ of the basic Ir-O-Ir bond attributable to individual lattice vibrational motions (from Ph1 to Ph7).

Phonon renormalization was consistent with the deviations in the Ir-O-Ir bond angle $\Delta\theta/\theta_0$, but the length changes $\Delta l/l_0$ did not fit the experimental results, especially in the cases of Ph4 and Ph7. Note that $\Delta\theta/\theta_0$ becomes the largest for Ph6. This behavior suggests that the unusual phonon renormalization in $Y_2Ir_2O_7$ is closely related to the modulation of the Ir-O-Ir bond angle.

Ultimately, we found that changes in the Ir-O-Ir bond angle explained the observed phonon renormalizations; bond length changes played only minor roles. In $Y_2Ir_2O_7$, the Ir-O bond length change Δl has only a slight effect on $\Delta\omega_0$. We calculated the length changes $\Delta l/l_0$ associated with each phonon mode and found that they deviate markedly from the experimental results, especially for Ph4 and Ph7. Additionally, if Δl is indeed the critical parameter for the phonon renormalization, the stretching modes would be expected to show

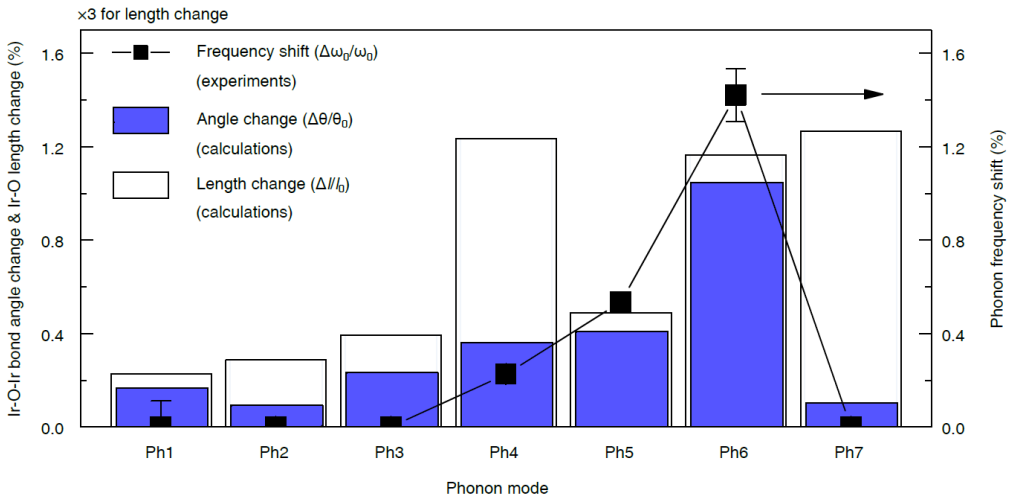

Figure 7. Relevance of variations in the Ir-O-Ir bond angle $\Delta\theta$ to phonon renormalization $\Delta\omega_0$. For all phonon modes, $\Delta\theta$ varied in a manner similar to $\Delta\omega_0$, but Δl appeared to be not directly affected (especially in the cases of Ph4 and Ph7). To facilitate direct comparison, the values plotted in this figure are dimensionless and the rescaled Δl is reduced by a factor of three.

the largest frequency shifts. However, the stretching mode Ph7 shows no frequency shift near T_N. These observations indicate that Δl cannot play important roles in $\Delta\omega_0$ at T_N.

3.4.2 Tight biding model calculations

To elucidate the microscopic origin of SPC in $Y_2Ir_2O_7$, we meticulously examined the relation between $\Delta\omega_0$ and $\Delta\theta$. The bond angle change induced by lattice vibration can affect the H_{spin} in $Y_2Ir_2O_7$, given in equation (1). Due to the strong SOC in pyrochlore iridates, the low energy magnetic degrees of freedom may be represented by pseudospins, $J_{eff} = 1/2$. Previous studies have also concluded that the AE interaction is at least an order of magnitude smaller than the other terms in H_{spin}. Consequently, for $Y_2Ir_2O_7$, $\Delta\omega_0$ may be largely

attributed to the IE and DM interactions:

$$\Delta\omega_0 \cong \frac{2}{I\omega_0}\left(\sum_{i,j}^{nn}\frac{\partial^2 J_{IE_{ij}}(\theta)}{\partial\theta^2}\langle \mathbf{S}_i\cdot\mathbf{S}_j\rangle + \sum_{i,j}^{nn}\frac{\partial^2 \mathbf{D}_{ij}(\theta)}{\partial\theta^2}\cdot\langle \mathbf{S}_i\times\mathbf{S}_j\rangle\right), \quad (17)$$

where I is the rotational inertia of the given phonon. The positive or negative sign of $\Delta\omega_0$ determines whether the corresponding phonon softens or hardens.

To compare the contributions of the IE and DM interactions quantitatively, we considered a tight-binding model based on O-mediated Ir-Ir hopping. Previous tight-binding models for pyrochlore iridates assumed that Ir-O hopping could occur along the local axes. However, the actual lattice structure includes a strong trigonal distortion of the O octahedra even though the global lattice symmetry is maintained. This distortion moves the O ion position away from the local axes of Ir ions (i.e., along the z_L and y_L axes in the Fig. 8a. Figure 8a show the changes of Ir-O-Ir bond during the trigonal distortion. Note that when the Ir-O-Ir bond angle changes to θ_0, the Ir-O hopping is no longer aligned to the local axes.

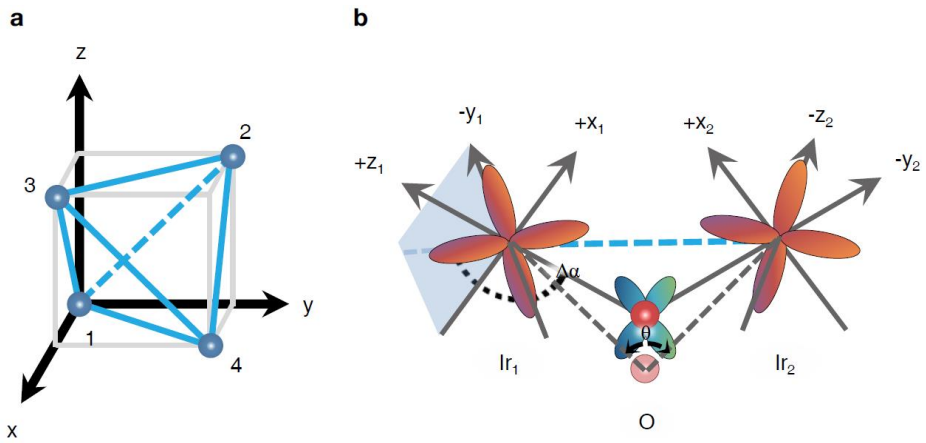

Figure 8. Structure distortion of octahedra and corresponding bond angle change in the pyrochlore lattice. a Structure of the pyrochlore lattice. Four Ir ions sit at each vertex of a tetrahedron. Each site within a tetrahedral unit cell is numbered from 1 to 4. b Oxygen-mediated hopping between Ir ion sites. θ is the Ir-O-Ir bond angle ang α is the Ir-Ir-O bond angle. Without breaking global lattice symmetry, the trigonal distortion of octahedra causes oxygen ion displacement from the Ir local axes.

We derive $J_{IE}(\theta)$ and $D(\theta)$ in the spin Hamiltonian, both of which are required for the calculation of $\Delta\omega_0$. We used the effective hopping Hamiltonian derived by Pesin and Balents [12]. We considered electron hopping between the nearest-neighbor Ir ions, which primarily contributes to J_{IE} and D [9,12]. As shown in the main text, the Ir-O-Ir bond is a key element whose O ion plays an important role in determining O-mediated hopping processes. The O ion displacement could modulate hopping, resulting in the bond angle θ dependence of J_{IE} and D.

First, we introduce the effective hopping Hamiltonian [12]:

$$H_{eff} = \sum_{\substack{\langle Ri,R'i'\rangle \\ \gamma\gamma'}} d^{\dagger}_{Ri\gamma} \boldsymbol{T}^{ii'}_{\gamma\gamma'} d_{R'i'\gamma'} + h.c., \tag{18}$$

where $\boldsymbol{T}^{ii'}_{\gamma\gamma'}$ (or simply $\boldsymbol{T}$) is the hopping matrix between the nearest-neighbor Ir ions, and $d^{(\dagger)}_{Ri\gamma}$ is the annihilation (creation) operator of t_{2g} orbitals. Subscripts R and i label the unit cell site and Ir site in the tetrahedron, respectively. An additional subscript γ was introduced to assign two levels of the $J_{eff} = 1/2$ doublet separately.

We derived the hopping matrix T, which is comprised of O-mediated hopping, $\boldsymbol{T}_{oxy}$, and direct hopping, $\boldsymbol{T}_{dir}$: $\boldsymbol{T}(\theta) = \boldsymbol{T}_{oxy}(\theta) + \boldsymbol{T}_{dir}$. The O displacement causes $\boldsymbol{T}_{oxy}$ to be dependent on the bond angle θ, whereas $\boldsymbol{T}_{dir}$ is nearly independent of θ [9]. We obtained $\boldsymbol{T}_{oxy}(\theta)$, considering both the rotation from Ir local axes to global axes and the octahedral distortion against the local axes:

$$\left[\boldsymbol{T}^{ii'}_{oxy}\right]_{\gamma,\gamma'} = \sum_{ll',\sigma\sigma'} \left[M^{\gamma}_{l\sigma}\right]^{*} M^{\gamma'}_{l'\sigma'} \left[\left[\boldsymbol{R}^{i}\boldsymbol{\tau}_{\boldsymbol{ii'}}(\theta)\right]^{T} \boldsymbol{R}^{i'}\boldsymbol{\tau}_{\boldsymbol{i'i}}(\theta)\right]_{ll'} \left[\left[\boldsymbol{D}^{(i)}\right]^{\dagger} \boldsymbol{D}^{(i')}\right]_{\sigma\sigma'}, \tag{19}$$

where the rotation matrix $R^{(i)}$ is obtained by rotating the global cubic axis of the ith Ir atom

to the local octahedral axis. The matrix $D^{(i)}$ corresponds to a spinor representation of $R^{(i)}$. We denote these basic states as $|\gamma\rangle = \sum_{l\sigma} M_{\gamma,l\sigma}$, considering the transitions between $J_{\text{eff}} = 1/2$ doublet states.

To achieve the θ-dependent T_{oxy}, we derived the generalized hopping matrices, $\boldsymbol{\tau}_{ii'}(\theta)$, connecting ($p_x$, p_y, p_z) orbitals to (d_{yz}, d_{zx}, d_{xy}) orbitals. We assumed that $t_{pd\pi} = \frac{-1}{\sqrt{3}} t_{pd\sigma}$ [45]. Finally, $T_{ij}(\theta)$ can be expressed by a combination of Pauli matrices $\boldsymbol{\sigma}$:

$$\boldsymbol{T}^{ii'}(\theta) = t(\theta)\mathbb{I} + iv(\theta)\boldsymbol{d}_{ii'} \cdot \boldsymbol{\sigma}, \tag{20}$$

where $t(\theta) = a(\theta)t_{oxy} + bt_\sigma$ and $v(\theta) = a'(\theta)t_{oxy} + b't_\sigma$ [9], and $\boldsymbol{d}_{ii'}$ is a unit vector. The coefficients $a^{(\prime)}$, $b^{(\prime)}$ and vector $\boldsymbol{d}_{ii'}$ were obtained using Slater–Koster methods [46]. Therefore, t_{oxy} and t_σ are the only remaining unknown parameters.

To calculate $\Delta\omega_0$, we need J_{IE} and D as functions of θ. A microscopic model provides J_{IE} and D [12]:

$$J_{\text{IE}}(\theta) = \frac{4}{U}\left(t^2(\theta) - \frac{1}{3}v^2(\theta)\right), \tag{21}$$

$$D(\theta) = \frac{8}{U}t(\theta)v(\theta). \tag{22}$$

By inserting $t(\theta)$ and $v(\theta)$ above, we obtain two quadratic equations for (t_σ/t_{oxy}):

$$\frac{D(\theta)}{J_{\text{IE}}(\theta)} = \frac{2\left(a(\theta)+b\frac{t_\sigma}{t_{oxy}}\right)\left(a'(\theta)+b'\frac{t_\sigma}{t_{oxy}}\right)}{\left(a(\theta)+b\frac{t_\sigma}{t_{oxy}}\right)^2 - \frac{1}{3}\left(a'(\theta)+b'\frac{t_\sigma}{t_{oxy}}\right)^2}, \tag{23}$$

$$D(\theta) = \frac{8}{U}\left(a(\theta) + b\frac{t_\sigma}{t_{oxy}}\right)\left(a'(\theta) + b'\frac{t_\sigma}{t_{oxy}}\right). \tag{24}$$

Only one solution satisfying the condition $D(\theta) < 0$ can stablize the AIAO magnetic ordering in pyrochlore iridates [12].

To make a quantitative comparison between $J_{IE}(\theta)$ and $D(\theta)$ for $Y_2Ir_2O_7$, we need to anchor their values for at least one angle. Unfortunately, experimental values have not yet been reported for $Y_2Ir_2O_7$. We therefore rely on a previous quantum chemistry calculation (QCC) study that computed $J_{IE}(\theta)$ (= 18.8 meV) and $D(\theta)$ (= 2.6 meV) at the experimentally determined angle θ_0^{QCC} (= 130°).

Using these QCC values, we quantitatively determined $J_{IE}(\theta)$ and $D(\theta)$. We finally acquired θ-dependent $J_{IE}(\theta)$ and $D(\theta)$ for $Y_2Ir_2O_7$ by anchoring it to the quantum chemical calculation results (i.e., J_{IE} = 18.8 meV and D = –2.6 meV at θ_0^{QCC} = 130°), yielding t_{oxy} ≈ 261 meV and t_σ ≈ –12 meV [47].

With proper consideration of the ionic position changes, we analytically obtained the θ-dependent Ir-O-Ir hopping. Then, using the Slater-Koster tables, we derived the bond angle-dependent coefficients $J_{IE}(\theta)$ and D(θ) (= $\|D_{ij}(\theta)\|$) in H_{spin}.

Using the $J_{IE}(\theta)$ and $D(\theta)$ values, we then estimated the IE and DM interaction energies $E_{IE} = J_{IE_{ij}}(\theta)\langle S_i \cdot S_j\rangle$ and $E_{DM} = D_{ij}(\theta)\cdot\langle S_i \times S_j\rangle$. By taking the second derivatives, i.e., the $\partial^2 E_{DM}/\partial\theta^2$ and $\partial^2 E_{IE}/\partial\theta^2$, we can compare both the IE and DM contributions to $\Delta\omega_0$ using equation (17). The results suggest $\partial^2 E_{DM}/\partial\theta^2 \approx 1.00$ eV/radians^2 and $\partial^2 E_{IE}/\partial\theta^2 \approx -0.09$ eV/radians^2 at θ = 130°. The contribution to phonon renormalization of the DM interaction ($\partial^2 E_{DM}/\partial\theta^2$) is therefore about an order of magnitude greater than that of the IE interaction ($\partial^2 E_{IE}/\partial\theta^2$). The dominance of the DM interaction is robust even when the anchoring values of $J_{IE}(\theta)$ and $D(\theta)$ were varied significantly. The DM interaction therefore plays a key role in the unconventional SPC observed in $Y_2Ir_2O_7$.

3.5 Conclusion

In this chapter, we show the phonon renormalization due to DM interaction in $Y_2Ir_2O_7$ using IR spectroscopic technique. Using the FTIR spectroscopy and spectroscopic ellipsometry, we obtain the temperature-dependent optical spectra. Based on these spectra with peak fitting process, we found the phonon renormalization of phonon frequencies. Combined with the DFT calculations, tight-binding model analysis provide us the origin of phonon renormalization, spin-phonon coupling via DM interaction. We expect that similar phenomena should be observed in other materials with large SOC and highly non-collinear spin ground states.

Chapter 4

Result and Discussion II:

Raman spectroscopy

Topological magnon bands are characterized by nodal points at linear magnon band crossing, analogous to Dirac (or Weyl) points in a fermionic topological system. Previously, as evidence of exotic topological feature, triply-degenerate point in linear band crossing structure has not been experimentally reported among pyrochlore iridates so far. Here, based on the Raman experiment and tight-binding calculations, we analyzed the spin Hamiltonian and magnetic excitations of $Y_2Ir_2O_7$. As a result, we demonstrate that $Y_2Ir_2O_7$ is the first candidate to have magnon band crossing in pyrochlore iridates.

4.1 Introduction

4.1.1 Brief history of magnon topology in pyrochlore lattice system

Recent theoretical studies have been focused on searching for bosonic topological materials, particularly with topological MB [48–51]. Such materials can be fundamentally interesting and have potential spintronic applications [52]. It was proposed that topological MB crossing, which can form a Weyl point, appears in limited non-centrosymmetric crystals or pyrochlore ferromagnets [49,50].

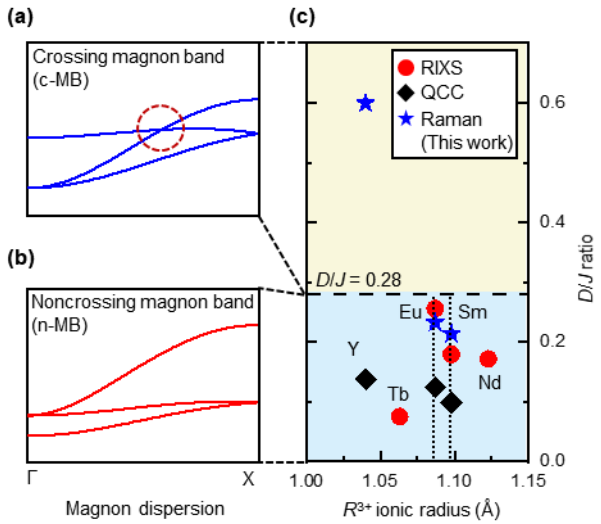

Figure 9. a-b Dispersions for crossing magnon band (c-MB) and noncrossing magnon band (n-MB). c Magnon band topology phase diagram for some pyrochlore iridates $R_2Ir_2O_7$ (R=Y, Tb, Eu, Sm, and Nd). We note that D/J= 0.28 in Ref. [53] is the boundary between the c-MB and n-MB topology, where the Dzyaloshinskii-Moriya interaction and the Heisenberg interaction are denoted by D and J, respectively. Red dots are parameters obtained from resonant inelastic X-ray scattering (RIXS) experiments and black diamonds are parameters from quantum chemistry calculations (QCC). For $Nd_2Ir_2O_7$ and $Tb_2Ir_2O_7$, the QCC may be less accurate because of the incorrect Ir-O-Ir angles. Therefore, the QCC parameters for $Nd_2Ir_2O_7$ and $Tb_2Ir_2O_7$ are excluded. Our Raman data (blue star) suggest $Y_2Ir_2O_7$ is in the c-MB phase, contrary to the result of the QCC.

However, topological MB crossing was later observed in the so-called three-dimensional spin-web compounds with a collinear antiferromagnetic order [51,52].

The pyrochlore iridate $R_2Ir_2O_7$ can be an interesting material system with noncollinear antiferromagnetism and a possible change in topological MB structure. By varying small structural details with R, we can modulate magnetic interactions, which determine dispersion of MB. Recently, Hwang *et al*. [53] theoretically suggested that MB topology changes in $R_2Ir_2O_7$. Their calculation shows the 4 lowest-lying MBs, which have singly and triply degeneracies at Γ. As shown in Fig. 9a, when the triply-degenerate band at Γ is located at lower energy, the MBs make a crossing at some $\boldsymbol{k}$ along the Γ to X lines (i.e. along with the six cubic directions). This case will be called a phase with a crossing magnon band (c-MB). On the other hand, as shown in Fig. 9b, when the triply-degenerate band at Γ is located at higher energy, the MBs will not make any crossing, which will be called a phase with the non-crossing MB (n-MB).

By using linear spin wave theory calculations, Hwang *et al*. [53] also claimed that the ratio between Dzyaloshinskii-Moriya (DM) interaction (D) and Heisenberg interaction (J) can be a key parameter for controlling MB topology. When $D/J < 0.28$, R227 will have n-MB. On the other hand, when $0.28 < D/J < 0.71$ [53], R227 will have c-MB. The distinct MB topology can lead to differences in Berry curvature, which can manifest as the magnon thermal Hall effects. Namely, the n-MB and c-MB phases are predicted to show positive and negative thermal Hall conductivity, respectively.

4.1.2 Brief history of magnon studies Raman spectroscopy

Inelastic neutron scattering is a conventional experimental technique for studying magnetic excitations. Because Ir^{4+} ions strongly absorb neutrons, this powerful technique cannot be applied to pyrochlore iridates. Instead, resonant inelastic X-ray scattering (RIXS) has often been used as an alternative [54–56]. However, the resolution of this experimental technique is 25–28 meV, which is much larger than the predicted energy difference of about 4 meV between the non-degenerate and triply-degenerate MBs at the Γ point in $R_2Ir_2O_7$ [53,54].

Theoretical quantum chemistry calculations (QCC) have been widely applied, but their calculational results are highly dependent on the Ir-O-Ir bond-angle (θ) [47]. We note that all reported D/J values for $R_2Ir_2O_7$ are located at the n-MB phase [Fig. 9c], suggesting the absence of the topological phase transition in $R_2Ir_2O_7$. In addition, the D/J values of each technique do not show systematic evolution with the variation in radius of rare-earth ions.

Raman spectroscopy is well suited to estimating the values of magnetic interactions and to investigation of the MB topology of $R_2Ir_2O_7$. Because of its high energy resolution (~ 0.2 meV), Raman spectroscopy can resolve fine structures from magnetic excitations and yield detailed information concerning magnetic interactions [11,57].

4.1.3 Brief history of magnon studies Raman spectroscopy

Conventional magnon scattering mechanism is based on the two-magnon scattering process in Raman spectroscopy. From the Fleury and Loudon's theory, electric-dipole transition on the nearest neighbor two site ion via exchange interaction induces the two-magnon scattering. This scattering process is proportional to the density of states for all k-space in Brillouin zone (BZ). In general, this scattering signal is easy to be found comparing to the single-magnon scattering, which can emerge on the Γ point of BZ.

Recently, enhanced signal due to single-magnon scattering process is reported for several materials. These materials, Ca_2RuO_4 and Sr_2IrO_4 [58,59], are well-known to be a pseudospin state. RIXS measurement for these materials are confirm to have a single-magnon energies on the same position of the Raman signal.

4.2 Experimental details

Raman spectroscopy experiments were conducted at 532 nm in backscattering geometry. The sample was mounted on an *xyz*-stage inside a closed-cycle Montana cryostat for low-temperature measurements. To avoid thermal heating, the laser power was maintained at 0.1 mW and the anti-Stokes signal was used to confirm the temperature [60]. The beam spot on the sample surface was approximately 2 μm in diameter. The spectrometer had a 2,400 g/mm grating, with an Andor CCD, providing a resolution of ~ 2 cm^{-1} (0.2 meV). High-quality polycrystalline $Y_2Ir_2O_7$ was synthesized using a solid-reaction method [61].

4.3 Spectroscopic investigation

4.3.1 Temperature dependent Raman spectra

Six Raman-active phonon modes were observed in the Raman spectrum of $Y_2Ir_2O_7$ at 10 K [Fig. 2(a)], consistent with factor group analysis for the Fd-3m space group [62,63]. We performed DFT calculations to assign the symmetry of phonon modes. The calculated and experimental phonon frequencies showed good agreement, allowing assignment of the observed phonon modes. The peaks at 346 and 520 cm^{-1} correspond to E_g and A_{1g} modes, respectively. The four other peaks at 324, 404, 560, and 720 cm^{-1} are associated with T_{2g} modes.

The Raman spectra of $Y_2Ir_2O_7$ showed two peaks below 300 cm^{-1} marked as M_1 and M_2, which, as discussed below, could not be assigned as phonon modes. These well-resolved sharp peaks were located at 231 cm^{-1} (28.6 meV) and 277 cm^{-1} (34.4 meV) for M_1 and M_2, respectively. The linewidth of M_2, the strong intensity peak, is about 17 cm^{-1}, comparable with the linewidths of the phonon modes A_{1g}, E_g, and T_{2g} (14 – 19 cm^{-1}). The AIAO magnetic ordering protects the cubic lattice symmetry of $R_2Ir_2O_7$ [64], suggesting that the M peaks are not associated with zone-folded phonon in the AFM state.

Table 1. Calculated and experimental phonon frequencies of $Y_2Ir_2O_7$ at 10 K.

	Phonon frequencies (cm^{-1})					
$Y_2Ir_2O_7$	$T_{2g}(1)$	E_g	$T_{2g}(2)$	A_{1g}	$T_{2g}(3)$	$T_{2g}(4)$
DFT	318.2	359.8	391.6	509.9	547.6	707.6
Experiment	324.6	346.3	404.2	519.8	559.7	720.0

In addition, previous X-ray and neutron diffraction studies of $R_2Ir_2O_7$ found no structural phase transitions [40,41], confirming that the M peaks are irrelevant to lattice distortions.

To further investigate the nature of the M peaks, we studied the T dependence of the Raman spectra of $R_2Ir_2O_7$ [Fig. 10b]. We found that the M peaks are visible only in the AFM state. The evolution of the M peaks is more clearly visible in the difference spectra I_T-I_{300K} shown in Fig. 10c. As T increases from 10 to 150 K, the M peaks are significantly suppressed and become indistinguishable above T_N. Figure 10d shows the T-dependent integrated intensities from the spectra I_T-I_{300K} of the M peaks (black squares) and magnetic susceptibilities (red circles). The integrated intensities of both peaks reveal anomalies at T_N, suggesting a magnetic origin of the M peaks.

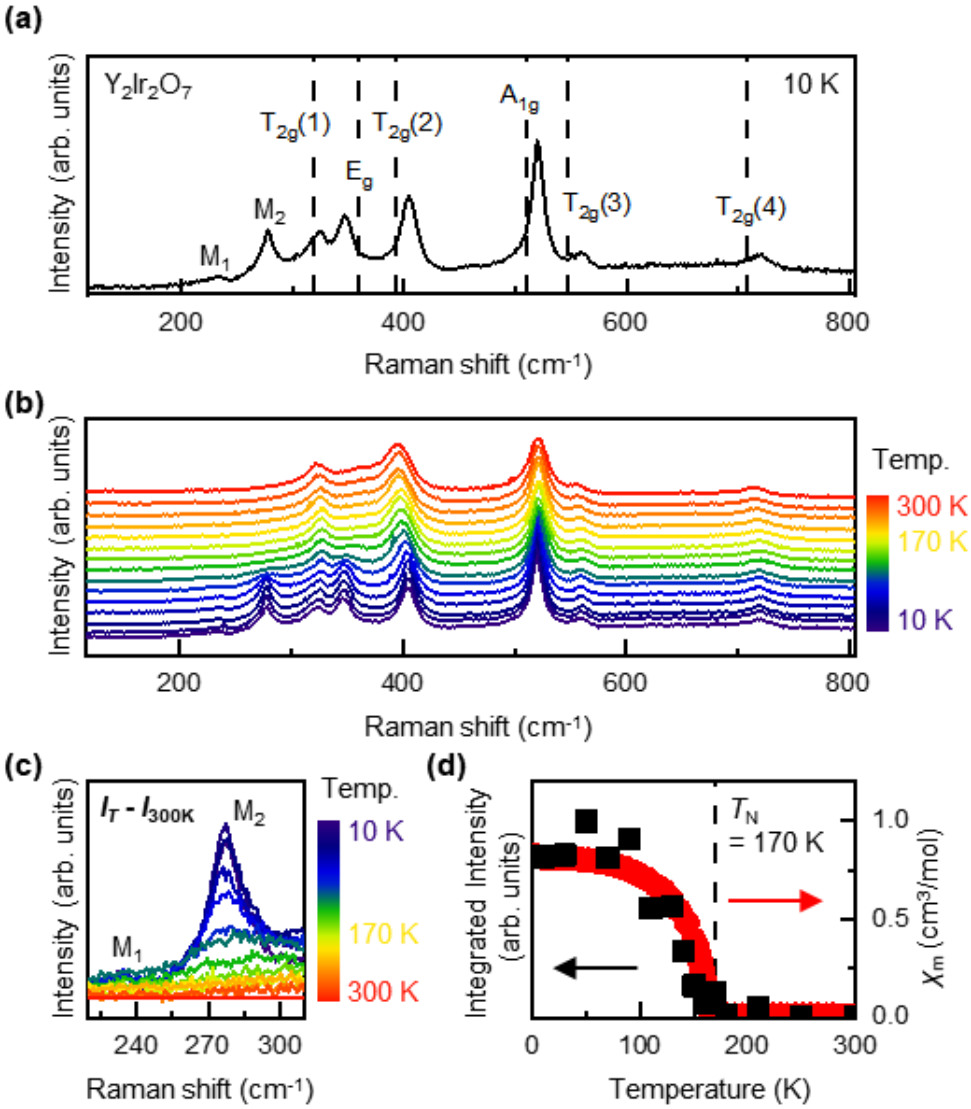

Figure 10. a Raman spectra of polycrystalline $Y_2Ir_2O_7$ at 10 K. The frequencies of the six Raman-active phonons are calculated using density functional theory calculations (solid lines). M_1 and M_2 correspond to magnetic excitations. b Temperature (T)-dependent Raman spectra of $Y_2Ir_2O_7$. c T-dependent Raman spectra of magnetic excitation peaks in $Y_2Ir_2O_7$. For clarity, each spectral intensity I_T at various T is subtracted by the intensity of reference spectrum I_{300} at 300 K. d T-dependence of the integrated intensity of the magnetic excitations in the range of 208 and 314 cm^{-1} (black squares) and magnetic susceptibility χ_m measured at H = 0.1 T after zero-field cooling (red circles). For integration, we subtracted the 300 K spectra from the spectra at the other temperatures and integrated them in the energy range between 208 and 314 cm^{-1}.

We carried out Raman spectroscopy measurements on $Sm_2Ir_2O_7$ and $Eu_2Ir_2O_7$ and found magnetic excitations, labeled as M_1 and M_2. Similar to $Y_2Ir_2O_7$, they showed the six Raman-active phonon modes above 300 cm^{-1}. Below 300 cm^{-1}, the new peaks M_1 and M_2 develop in the antiferromagnetic state. The M_1 and M_2 peak positions of $Sm_2Ir_2O_7$ and $Eu_2Ir_2O_7$ are 205.3 and 233.6 cm^{-1}, respectively, and those of $Eu_2Ir_2O_7$ were 212.4 and 234.3 cm^{-1}, which are consistent with previous reports [62,63]. The Raman spectra of $Sm_2Ir_2O_7$ [63] showed additional peaks at 88.8 and 267.5 cm^{-1}. These peaks could be attributed to the crystal field excitation of Sm^{3+} ions, as observed in $Sm_2Ti_2O_7$ and $Sm_2Zr_2O_7$.

The Raman spectra of $Sm_2Ir_2O_7$ and $Eu_2Ir_2O_7$ were reported previously [62,63]. Hasegawa et al. reported that new peaks appeared below the metal-to-insulator transition (MIT) temperature in the Raman spectra of $Sm_2Ir_2O_7$ and $Eu_2Ir_2O_7$ [63], and suggested that they reflected a structural phase transition. However, a later neutron powder diffraction study found no evidence of $R_2Ir_2O_7$ structural distortion across MIT and the magnetic transition T_N [40].

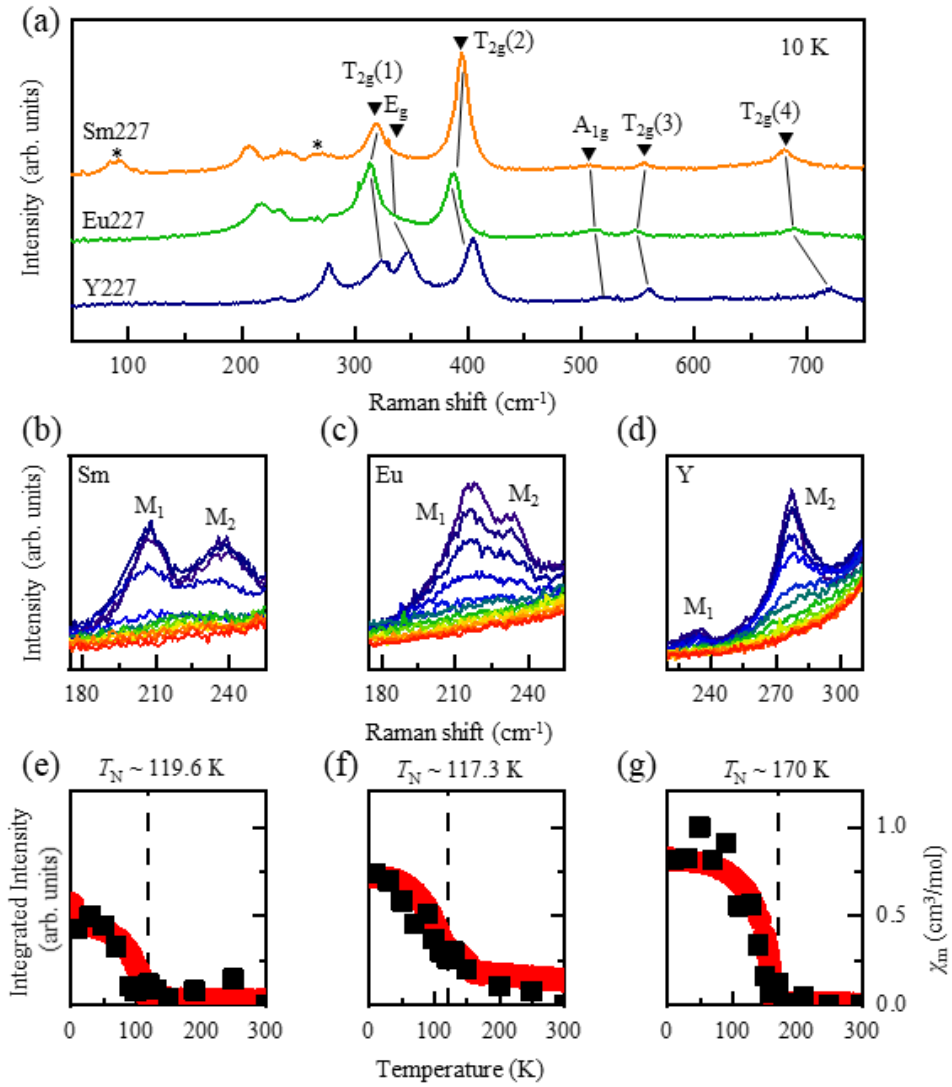

Figure 11. a Raman spectra of $R_2Ir_2O_7$ (R: Sm, Eu, Y) at low temperature (10 K). Using density-functional-theory calculations, we assigned the six Raman-active phonon modes located in the energy region above 300 cm^{-1}. Below 300 cm^{-1}, the Raman spectra of the three compounds commonly show two peaks that could be attributed to magnetic excitations. The peaks indicated by asterisks in the $Sm_2Ir_2O_7$ data may correspond to the crystal field splitting in Sm^{3+} ion. b-d T-dependent Raman spectra of magnetic excitation peaks (M_1 and M_2) in $R_2Ir_2O_7$. e-g Integrated intensities of M peaks (black squares) and magnetic susceptibility χ_m (red circles) of $R_2Ir_2O_7$. For integration, we subtracted the 300 K spectra from the spectra at the other temperatures and integrated them in the energy region between 208 and 314 cm^{-1}. χ_m are measured at H = 0.1 T after zero-field cooling.

4.3.2 Spin-wave dispersion of pyrochlore iridates

The magnon dispersion of the AIAO magnet has been studied extensively from a theoretical perspective. The fourfold-degenerate magnon dispersion in $R_2Ir_2O_7$ is strongly affected by the DM interaction, which exhibits a gap at the Γ point. Figure 3a summarizes the information related to MB for $Sm_2Ir_2O_7$, $Eu_2Ir_2O_7$, and $Y_2Ir_2O_7$. The red-colored regions indicate the bandwidth of MB from RIXS studies [54–56]. They indicate that the MB gap energies of $Sm_2Ir_2O_7$ and $Eu_2Ir_2O_7$ are ~ 25 and ~ 28 meV, respectively. To our knowledge, no experimental information concerning MB is available for $Y_2Ir_2O_7$ [40,65]. The energies of magnetic excitations of $Sm_2Ir_2O_7$ and $Eu_2Ir_2O_7$ from our Raman data are indicated by black solid lines in Fig. 3(a). Previous Raman studies of $Sm_2Ir_2O_7$ and $Eu_2Ir_2O_7$ also reported the magnetic excitation peaks at nearly the same energies [62,63]. The energies of the magnetic excitations of $Sm_2Ir_2O_7$ and $Eu_2Ir_2O_7$ are found to be close to their magnon dispersion gap energies.

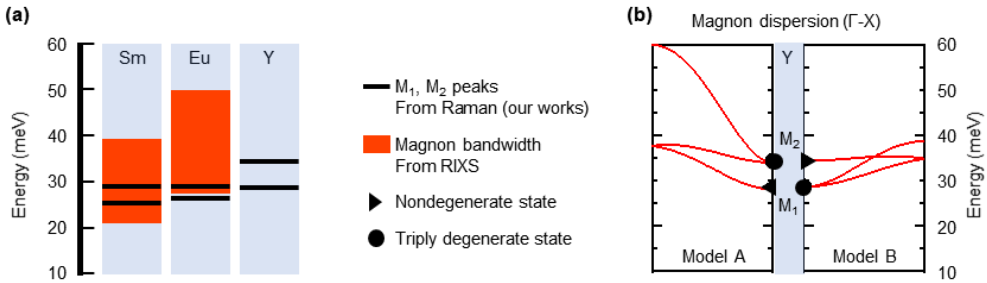

Figure 12. a Magnetic excitation energy diagram for $R_2Ir_2O_7$. Black lines indicate the energies of M_1 and M_2 from our Raman experiments. The magnon bandwidths obtained from the RIXS measurements are shaded in red [54–56]. b Magnon dispersion of $Y_2Ir_2O_7$ based on the linear spin-wave theory calculations with two Hamiltonian models in this work: Model A, where $J = 38.2$, $D = 6.9$ meV and nondegenerate (triangles) ≡ M_1, triply degenerate (circles) ≡ M_2 energy; and Model B, where for $J = 15.1$, $D = 9.0$ meV with triply degenerate ≡ M_1, nondegenerate ≡ M_2 energy.

These similarities suggest that the Raman peaks of $Sm_2Ir_2O_7$ and $Eu_2Ir_2O_7$ may correspond to 1MS.

Similarly, we attribute the M peaks in the Raman spectra of $Y_2Ir_2O_7$ to 1MS. Note that, in magnetic materials, Raman spectra usually show 2MS peaks, which are generally much stronger than 1MS peaks [66]. However, as shown in Fig. 12a-b, the resonance energies of the M peaks of $Y_2Ir_2O_7$ are close to the gap energies in the magnon dispersion of $Sm_2Ir_2O_7$ and $Eu_2Ir_2O_7$ as well as to the energies of 1MS in their Raman spectra [16–18, 26, 27]. In addition, the M peaks are much sharper (~ 17 cm^{-1}) than are the 2MS peaks (250–400 cm^{-1} for $R_2Ir_2O_7$) [11,58]. Symmetry analysis of the AIAO AFM state of $R_2Ir_2O_7$ further supports the conclusion that the M peaks are attributable to 1MS.

In general, the magnetic Hamiltonian for AIAO pyrochlore iridates can be written as:

$$\boldsymbol{H}_{spin=} \sum_{ij}^{\mathrm{nn}} (J\, \boldsymbol{S}_i \cdot \boldsymbol{S}_j + \boldsymbol{D}_{ij}\, (\boldsymbol{S}_i \times \boldsymbol{S}_j) + \boldsymbol{S}_i \cdot \mathbb{A}_{ij} \cdot \boldsymbol{S}_j), \tag{25}$$

where J and D are the Heisenberg and Dzyaloshinskii-Moriya interactions, respectively. Magnetic pyrochlore materials can also have anisotropic exchange interaction $\mathbb{A}$. Because $\mathbb{A}$ has values an order of magnitude smaller than J and D in $R_2Ir_2O_7$, we will focus on the J and D values in this paper. According to Ref. [53], the constraint on the nearest-neighbor $\mathbb{A}$ term can be calculated as:

$$\mathbb{A}_{ij}^{\alpha\beta} = \frac{D_{ij}^{\alpha} D_{ij}^{\beta}}{2J_{ij}} - \frac{\delta^{\alpha\beta} D_{ij}^{2}}{4J_{ij}}. \tag{26}$$

Thus, we can obtain $\mathbb{A}$ from J and D. Therefore, J and D can be directly computed. When the $\mathbb{A}$ term is included, the energies are slightly modified,

$$E_t = 2S\sqrt{\frac{\left(8\sqrt{2}(J+2\mathbb{A})+14\left(D-\frac{3\sqrt{2}}{4}\mathbb{A}\right)\right)\left(D-\frac{3\sqrt{2}}{4}\mathbb{A}\right)}{3}}, \tag{27}$$

$$E_s = 2S \cdot 3\sqrt{2}\left(D - \frac{3\sqrt{2}}{4}\mathbb{A}\right), \tag{28}$$

$$\mathbb{A} = \sqrt{J^2 + \frac{D^2}{3}} - J. \tag{29}$$

Table 2 presents a comparison of the J and D values with and without $\mathbb{A}$ for Models A and B described in the main text. We first note that the magnitude of $\mathbb{A}$ is very small: $\frac{\mathbb{A}_{xx}}{J} \approx 0.058$, $\frac{\mathbb{A}_{xx}}{D} \approx 0.098$. In addition, the inclusion of $\mathbb{A}$ has very small effects on the values of J and D; with changes of less than ~10%. According to Ref. [53], this does not markedly alter the magnon dispersion of $Y_2Ir_2O_7$.

Using simple equations, Hwang *et al*. derived the MB dispersions of $R_2Ir_2O_7$ [53]. At the Γ point the MB has triply- and singly-degenerate states with E_t and E_s, respectively. E_t and E_s can be expressed analytically in terms of J and D.

If the M peaks originate from the 1MS Raman process, they should correspond to E_s and/or E_t excitations. However, there are two possible scenarios for 1MS: E_s is smaller or larger than E_t. We considered both cases: Model A ($M_1 \equiv E_s$, $M_2 \equiv E_t$) and Model B ($M_1 \equiv E_t$, $M_2 \equiv E_s$). Using equations (27) and (28), we determined that $J = 37.6$ meV and $D = 7.0$ meV for Model A (and $J = 15.1$ meV and $D = 9.0$ meV for Model B).

Table 2. Comparison of the $Y_2Ir_2O_7$ spin parameters obtained via Raman scattering with and without consideration of anisotropic exchange.

Model	With $\mathbb{A}$			Without $\mathbb{A}$	
	J (meV)	D (meV)	$\mathbb{A}_{xx} = \mathbb{A}_{yy}$ (meV)	J (meV)	D (meV)
Model A	37.6	7.0	0.22	38.0	6.8
Model B	15.1	9.0	0.88	16.8	8.1

The magnon dispersions for Models A and B are plotted in Fig. 12b. The two models show very different MB dispersions: Model A indicates an n-MB phase and Model B indicates a c-MB phase. The *D*/*J* values of Models A and B are approximately 0.18 and 0.60, respectively.

Table 3. Magnetic interaction parameters for pyrochlore iridates $R_2Ir_2O_7$ (*R*=Y, Tb, Eu, Sm, and Nd)

Materials	θ	Study[a)]	J (meV)	D (meV)	D/J	Ref.
$Sm_2Ir_2O_7$	131.8 [67]	QCC	22.4	2.2	0.10	[47]
		RIXS	27.3	4.9	0.18	[54,55]
		Raman	29.2	6.2	0.21	Our work
$Eu_2Ir_2O_7$	130.7 [67]	QCC	19.3	2.4	0.12	[47]
		RIXS	40 (26.6)[b)]	- (6.8)[b)]	0.26	[56]
		Raman	27.9	6.5	0.23	Our work
$Tb_2Ir_2O_7$	-[c)]	QCC	-1.5	4.7	3.1	[47]
		RIXS	40	3	0.08	[54]
$Nd_2Ir_2O_7$	-[c)]	QCC	-1.6	5.1	3.1	[47]
		RIXS	28	4.8	1.7	[54]
$Y_2Ir_2O_7$	128.5 [40]	QCC	18.8	2.6	0.13	[47]
		NPD, RIXS	-	-	-	[40,65][d)]
		Raman	37.6	7.0	0.18	Model A
		Raman	15.1	9.0	0.60	Model B

a) QCC: quantum chemistry calculations; RIXS: resonant inelastic X-ray scattering; NPD: neutron powder diffraction
b) Ref. [56] described magnon dispersion without considering the Dzyaloshinskii-Moriya interaction. The values in parentheses are obtained by using equation (25) in the main text and the experimental RIXS results of $Eu_2Ir_2O_7$ in Ref [56].
c) The Ir-O-Ir bond-angles used in the QCC study [47] compared to those obtained by NPD for $Tb_2Ir_2O_7$ and $Nd_2Ir_2O_7$ [68,69].
d) Although NPD and RIXS experiments were conducted in Refs. [40,56], no evidence for magnetic excitations was found.

For comparison between pyrochlore iridate compounds, we provide the literature values of magnetic interaction parameters and structure information in Table 3, which we used in the main text. The values of magnetic interaction parameters are from the QCC study and RIXS studies. The Ir-O-Ir bond angles (θ) are derived from XRD and NPD measurements.

4.3.3 Single-magnon scattering mechanism in pseudospin J_{eff} =1/2 configuration

The pseudospin J_{eff}=1/2 configuration of $R_2Ir_2O_7$ can enable 1MS electric-dipole transition [66]. The conventional mechanism of the 1MS process is described by the magnetic-dipole transition as depicted in Fig. 13a.

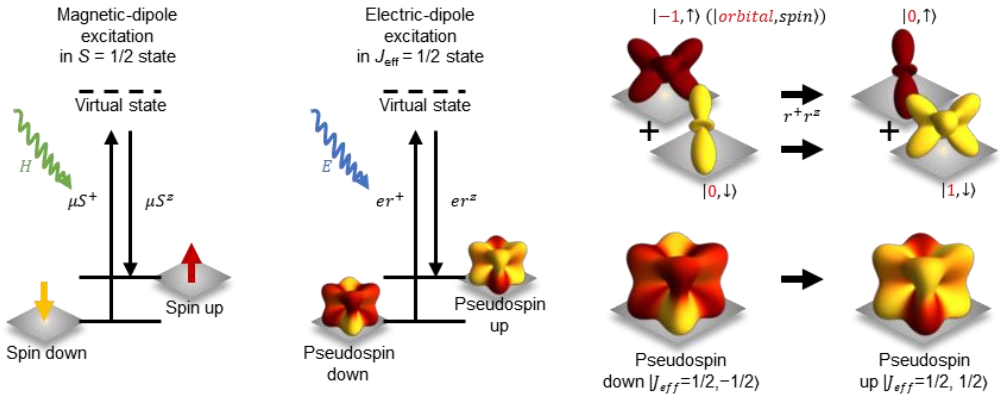

Figure 13. a Magnetic-dipole excitation in spin S=1/2 state. x and y components of the magnetic field ($H^{\pm}=H^{x}\pm iH^{y}$) operator creates the magnon and the H^{z} operator scatters the magnon. μ is the magnetic dipole moment of spin state. b Electric-dipole excitation in pseudospin J_{eff} = 1/2 state. Analogous to the magnetic-dipole transition, electric-dipole transition can create and scatter the magnon in pseudospin J_{eff} = 1/2 state configuration. An external E field can induce the electric-dipole (e·r) moment and modulate the pseudospin direction. The red and yellow area indicate the up and down spin states, respectively. c Pseudospin up and down configurations. The displacement operator of the electric-dipole transition term can change the orbital angular momentum by 1. The change in the orbital angular momentum can flip the pseudospin down state to the up state.

Magnetic-dipole Raman scattering occurs in the second-order perturbation process via $\boldsymbol{H_{MD}} = \boldsymbol{\mu}\sum \boldsymbol{S}\cdot\boldsymbol{H} = \boldsymbol{\mu}\sum(\frac{\boldsymbol{1}}{\boldsymbol{2}}[\boldsymbol{S^+H^-} + \boldsymbol{S^-H^+}] + \boldsymbol{S^zH^z})$ in the Hamiltonian. In the local coordinates, scattering (creation and destruction) of magnon operators is linear in the *z* (*x* and *y*) components of the radiational field [33]. The matrix element for the scattering process is proportional to $\langle\uparrow|S^{+(z)}|M\rangle\langle M|S^{z(+)}|\downarrow\rangle H^-H^z$, where $|M\rangle$ represents the intermediate state and $|\uparrow\rangle$ ($|\downarrow\rangle$) represents the spin-up (spin-down) state. However, 1MS caused by magnetic-dipole scattering has rarely been observed due to extremely small scattering efficiency. Conversely, in pseudospin configuration, the electric field can couple to the magnon operators via $H_{ED} = e\sum(r\cdot E) = e\sum(\frac{1}{2}[r^+E^- + r^-E^+] + r^zE^z)$ as described in Fig. 13b. The second order perturbation process is proportional to $\langle\tilde{\uparrow}|r^{+(z)}|M\rangle\langle M|r^{z(+)}|\tilde{\downarrow}\rangle E^-E^z \sim \langle\tilde{\uparrow}|S^+|\tilde{\downarrow}\rangle E^-E^z$, where $|\tilde{\uparrow}\rangle$ ($|\tilde{\downarrow}\rangle$) corresponds to the J_{eff} = 1/2 pseudospin-up (pseudospin-down) state [10]. This electric-dipole transition alters the unquenched orbital angular momentum of the pseudospin state $|\tilde{\downarrow}\ (\tilde{\uparrow})\rangle = \frac{\pm 1}{\sqrt{3}}|0,\downarrow\ (\uparrow)\rangle + \sqrt{\frac{2}{3}}|\mp 1,\uparrow\ (\downarrow)\rangle$ by ±1. As shown in Fig. 13c, the change in orbital angular momentum flips the pseudospin direction, leading to 1MS.

We consider the microscopic process of single-magnon scattering in pseudospin configuration. The electric-dipole scattering process is driven by the $H_{ED} = e\sum(r\cdot E) = e\sum\left(\frac{1}{2}[r^+E^- + r^-E^+] + r^zE^z\right)$, where *e*, *r*, and *E* indicate the charge of the electron, ionic displacement from the equilibrium position, and radiational electric field, respectively. Within the second-order time-dependent perturbation theory, the scattering matrix is given

by

$$\Gamma_{\text{Stokes}} = \sum_{M} \left[\frac{\langle \tilde{\downarrow} | er^z | M \rangle \langle M | er^- | \tilde{\uparrow} \rangle E_S^z E_I^+ - \langle \tilde{\downarrow} | er^- | M \rangle \langle M | er^z | \tilde{\uparrow} \rangle E_S^+ E_I^z}{(\hbar\omega_I - \hbar\omega_S - \hbar\omega_0)^2} \right.$$

$$\left. - \frac{\langle \tilde{\downarrow} | er^z | M \rangle \langle M | er^+ | \tilde{\uparrow} \rangle E_S^z E_I^- - \langle \tilde{\downarrow} | er^+ | M \rangle \langle M | er^z | \tilde{\uparrow} \rangle E_S^- E_I^z}{(\hbar\omega_I - \hbar\omega_S - \hbar\omega_0)^2} \right], \quad (30)$$

where the $|\tilde{\uparrow}\rangle$ and $|\tilde{\downarrow}\rangle$ is J_{eff}=1/2 pseudospin up and down states, respectively, and ω_I (ω_S) is the incident (scattered) photon frequencies [66,70]. $\hbar\omega_0$ indicates the Raman excitation energy from the ground state. In the pseudospin J_{eff}=1/2 configuration, for the anticommutative relation between the incident and scattered operators:

$$\langle \tilde{\downarrow} | r^z | M \rangle \langle M | r^{\mp} | \tilde{\uparrow} \rangle = -\langle \tilde{\downarrow} | r^{\mp} | M' \rangle \langle M' | r^z | \tilde{\uparrow} \rangle \sim \langle \tilde{\downarrow} | S^{\mp} | \tilde{\uparrow} \rangle. \quad (31)$$

The Stokes scattering matrix is obtained as follows:

$$\Gamma_{\text{Stokes}} \sim \frac{\langle \tilde{\downarrow} | \{ (E^z E^+ + E^+ E^z) S^- - (E^z E^- + E^- E^z) S^+ \} | \tilde{\uparrow} \rangle}{(\hbar\omega_S - \hbar\omega_I - \hbar\omega_0)^2}, \quad (32)$$

The above formula is valid within the framework of the local axes. It is necessary to consider the different local axes for the four sublattices in the unit cell for the pyrochlore lattice system with all-in-all-out magnetic ordering. Using the rotation matrix Λ_i, we can transfer each local coordinate to the global coordinate matrix form [53]. Then, we can integrate the total scattering matrix for each sublattice.

The symmetry of the Raman scattering matrix for each magnon excitation state is obtained by linear spin-wave theory calculations [53]. Using the linearized Holstein-Primakov representation, we can obtain the magnon creation annihilation operator $\{a^\dagger, a\}$ transferred from the spin operators $\{S^+, S^-\}$: $S^+ = \sqrt{2S}a,\ S^- = \sqrt{2S}a^\dagger,\ S^z = S - aa^\dagger$. The magnon Hamiltonian is diagonalized via the Bogoliubov transformation that relates the

magnon bosonic operator $a^{\dagger}(a)$ with magnon quasiparticle modes: $b_j^{\dagger} = \sum_i (c_i a_i^{\dagger} + d_i a_i)$, where *i* and *j* indicate the spin sublattices and each quasiparticle mode, respectively. Based on this transformation, the spin representation $\langle \tilde{\downarrow} | S^{\mp} | \tilde{\uparrow} \rangle$ is replaced by the magnon quasiparticle representation $\langle e | b^{\dagger} | g \rangle = \sum_i \langle e | (c_i a_i^{\dagger} + d_i a_i) | g \rangle$, where $|g\rangle$ and $|e\rangle$ are the magnon ground and excited state, respectively. Combined the linearized Holstein-Primakov representations and equation (25), we can obtain eigenvalues and eigenvectors for four magnon states. In Ref. [53], detailed information and the resulting Hamiltonian matrixes are provided. The Bogoliubov transformation to the magnon scattering matrix is used to derive the matrix elements for each magnon state.

For singly-degenerate state, for example, magnon quasiparticle operator $b^{\dagger}$ can be represented by the coefficient set: $\{c_i, d_i\}=\{1/2, -\omega^2/2, 1/2, -\omega^2/2, 0, 0, 0, 0\}$. The Raman scattering matrix is represented by the from:

$$[\Gamma_{\text{Stokes}}]_{\alpha\beta} \sim |E|^2 \sum_i \left[\frac{\left([\Lambda_i \cdot \epsilon^z]_\alpha [\Lambda_i \cdot \epsilon^+]_\beta + [\Lambda_i \cdot \epsilon^+]_\alpha [\Lambda_i \cdot \epsilon^z]_\beta\right) \langle e | c_i a_i^{\dagger} | g \rangle}{(\hbar\omega_I - \hbar\omega_S - \hbar\omega_0)^2} \right.$$

$$\left. - \frac{\left([\Lambda_i \cdot \epsilon^z]_\alpha [\Lambda_i \cdot \epsilon^-]_\beta + [\Lambda_i \cdot \epsilon^-]_\alpha [\Lambda_i \cdot \epsilon^z]_\beta\right) \langle e | d_i a_i | g \rangle}{(\hbar\omega_I - \hbar\omega_S - \hbar\omega_0)^2} \right] \tag{33}$$

Based on the equation (33), rotation matrix Λ_i, and magnon quasiparticle eigenstate, the Raman scattering matrix is derived as

$$\Gamma_{\text{Stokes}} \sim B \begin{pmatrix} \omega^* & 0 & 0 \\ 0 & \omega & 0 \\ 0 & 0 & 1 \end{pmatrix}. \tag{34}$$

The magnetic point group for $R_2Ir_2O_7$ is $m3m'$, so there are three possible Raman tensors with symmetries A_g, E_g, and T_g [71]. The matrix representation in equation (34) is the same

as the Raman tensor of E_g symmetry. Similarly, for the triply-degenerate state, we obtained the Raman tensor of T_g symmetry.

A_g and E_g are for parallel polarization and T_g is for cross-polarization symmetry. For $\boldsymbol{J}_{eff}$=1/2 configuration in AIAO ordering, we found E_g and T_g symmetry for singly and triply degenerate state, respectively. A previous Raman study on $Eu_2Ir_2O_7$ single-crystal indeed showed that the strong magnetic peak appears in E_g symmetry, which supports our symmetry analysis results [62].

As the Raman scattering efficiency is proportional to the square of the scattering matrix Γ_{Stokes} [66], the efficiencies of magnetic and electric-dipole transitions are proportional to the dipole interactions to the power of four. Using these relations, we can simply compare the Raman intensities between two different dipole scatterings. Starting from the ratio between electric and magnetic-dipole interactions,

$$r_{e-m} = \left|\frac{\langle PE\rangle}{\langle \mu B\rangle}\right|^4 = \left|\frac{\langle erE\rangle}{\langle \mu B\rangle}\right|^4 , \tag{35}$$

where P is the electric dipole moment, μ is magnetic dipole moment, e is the charge of an electron, and r is the ionic displacement from the equilibrium position. E and B indicate the radiational field of the electromagnetic wave. In general, $\langle r\rangle$ is the scale of the Bohr radius, a_B, in solid. In addition, the magnetic moment of ions is the scale of Bohr magneton μ_B. From the electromagnetic wave equation in a vacuum, we obtained a relation between electric and magnetic radiational field, $E = cB$ [66]. Assuming that $\langle r\rangle \sim a_B$ and $\langle \mu\rangle \sim \mu_B$ $r_{e\text{-}m}$, we have

$$\left|\frac{\langle erE\rangle}{\langle \mu B\rangle}\right|^4 \sim \left|\frac{ea_B cB}{\mu_B B}\right|^4 = \left|\frac{ea_B c}{\mu_B}\right|^4 . \tag{36}$$

Using the equation $\mu_B = \frac{e\hbar}{2m_e}$, $a_B = \frac{\hbar}{m_e c\alpha}$, and the fine-structure constant $\alpha \cong 1/137$, we simplify $r_{e\text{-}m}$ as follows:

$$r_{e-m} \sim \left|\frac{2m_e a_B c}{\hbar}\right|^4 = \left(\frac{2}{\alpha}\right)^4 \sim 5.64 \times 10^9. \quad (37)$$

As a result, the intensity of Raman scattering efficiency from the electric-dipole transition is larger by a factor of 9 larger than that of magnetic-dipole transition.

4.4 Theoretical calculation

4.4.1 Tight-binding model estimations

To further confirm that Model B correctly describes the magnon dispersion, we performed tight-binding calculations on the Ir-O-Ir angle (θ) dependence of J and D in $R_2Ir_2O_7$. Electron hopping between the nearest neighbor Ir ions contributes to J and D. In $R_2Ir_2O_7$, the hopping integral depends on θ, thus affecting the J and D values. We used the θ values of the $R_2Ir_2O_7$ compounds from the previous X-ray diffraction (XRD) and neutron diffraction studies [40,67]. Details of the θ dependence of J and D are provided in Ref. [61].

In our previous study on the IR-active phonon modes of Y227 [61], we used tight-binding calculations to show that the anomalous IR phonon softening was principally attributable to spin-phonon coupling (SPC) via a Dzyaloshinskii-Moriya (DM) interaction. We employed the values of J = 18.8 meV, D = 2.6 meV, and θ = 130° of the quantum chemical calculation (QCC) study [47] as anchoring points for the θ-dependent J and D calculations.

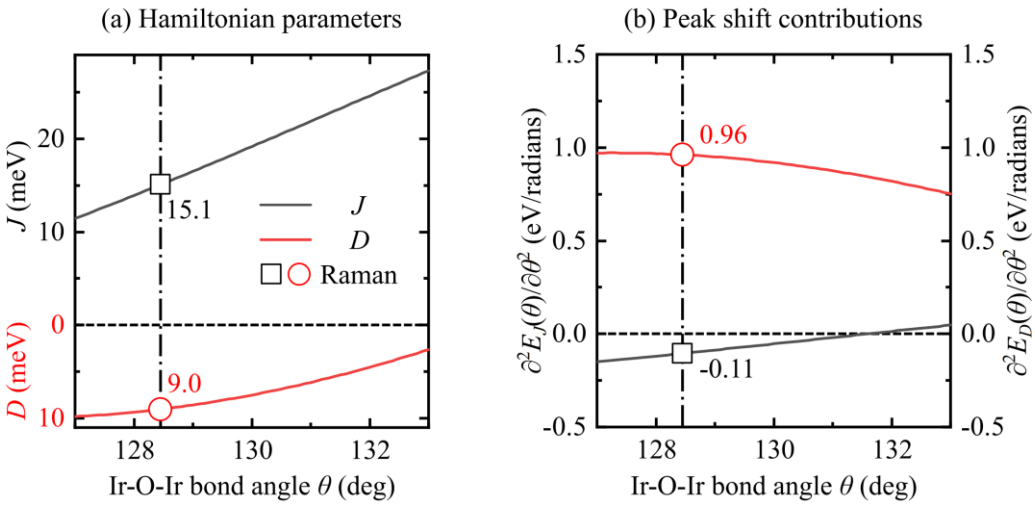

Figure 14. Spin-phonon coupling contributions due to Heisenberg and Dzyaloshinskii-Moriya interactions. a θ-dependent J and D curves calculated using the tight-binding model using the anchoring points J = 15.1 meV, D = 9.0 meV, and θ = 128.5°. b The second derivatives of $E_J = J(\theta)\langle S_i \cdot S_j \rangle$ and $E_D = D_{ij}(\theta)\langle S_i \times S_j \rangle$.

In the current work, we extracted the *J* and *D* values (*J* = 15.1 meV, *D* = 9.0 meV) from Raman spectra. Here we reexamine whether the DM interaction triggers SPC; using the Raman data. We estimate the contributions of *J* and *D* to A_{1g} phonon-softening by calculating the second derivatives of θ-dependent *J* and *D*. We use *J* = 15.1 meV and *D* = 9.0 meV as an anchoring point. We also employ an Ir-O-Ir bond angle θ of 128.5° as an anchoring point. The θ value was determined in a neutron powder diffraction study [40] and is more reliable for refining the oxygen position than the XRD angle [40,67].

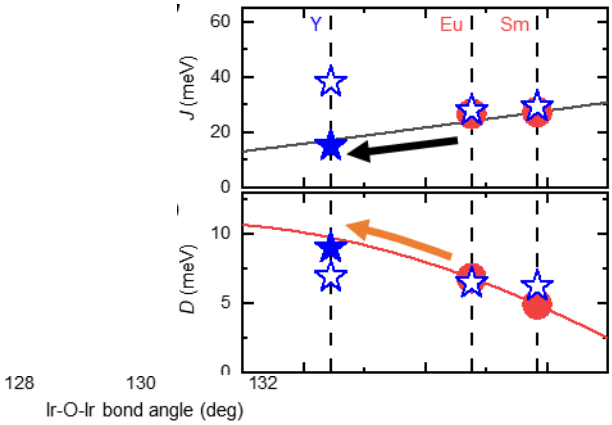

Figure 15. a-b Ir-O-Ir bond-angle (θ) dependence of J and D obtained from tight-binding calculations on $R_2Ir_2O_7$ (R: Sm, Eu, Y). The calculated curves of $J(\theta)$ and $D(\theta)$ agree with the J and D values in Model B for $Y_2Ir_2O_7$ but differ markedly from the J and D values in Model A. Conversely, the calculated curves agree with the J and D values in Model A for $Sm_2Ir_2O_7$ and $Eu_2Ir_2O_7$, i.e. they have n-MB topology. Our results indicate that $Y_2Ir_2O_7$ is the only candidate in the $R_2Ir_2O_7$ system to have c-MB topology.

In Fig. 15a-b, we compare the tight-binding calculation results for $Y_2Ir_2O_7$, $Eu_2Ir_2O_7$, and $Sm_2Ir_2O_7$ with those from previous RIXS studies [54–56]. We did not include $Nd_2Ir_2O_7$ and $Tb_2Ir_2O_7$ [68,69], because their bond lengths are quite different from the bond lengths of the other pyrochlore iridates (e.g., $Y_2Ir_2O_7$, $Eu_2Ir_2O_7$, and $Sm_2Ir_2O_7$) [40,67]. The empty and solid stars correspond to J and D values for Models A and B, respectively. The calculations of the θ dependence of J and D indicate that Model B (J = 15.1 and D = 9.0 meV) can appropriately represent the magnetic excitations in $Y_2Ir_2O_7$.

4.4.2 Spin-phonon coupling in Raman spectroscopy

To determine which of these models is correct, we investigated the T dependence of Raman-active phonon peaks. In our earlier IR spectroscopy study of $Y_2Ir_2O_7$ indicated that

the three phonon modes show anomalous softening below T_N, attributable to SPC [61]. In a previous study [61], we showed that the Ir-O-Ir bending motion (in the Ir-O-Ir plane) is strongly correlated with the θ-dependent J and D modulation. In Fig. 16, for the A_{1g} mode, all oxygen ions between the nearest-neighboring Ir ions move within the Ir-O-Ir plane and perpendicular to the Ir-Ir bond, creating a bending motion. Thus, the ionic vibration of the A_{1g} modes of our Raman spectra induces obvious changes in the Ir-O-Ir angles, thereby modulating J and D, and exhibiting the largest softening.

As shown in Fig. 17a, our Raman spectra of the A_{1g} mode show similar phonon softening below T_N. The atomic displacement of the A_{1g} mode is depicted in Fig. 16b. To obtain quantitative information, we fit the A_{1g} mode by using the Lorentzian lineshape. The T evolution of the Raman shift is shown in Fig. 17c. Above T_N, the A_{1g} phonon frequency

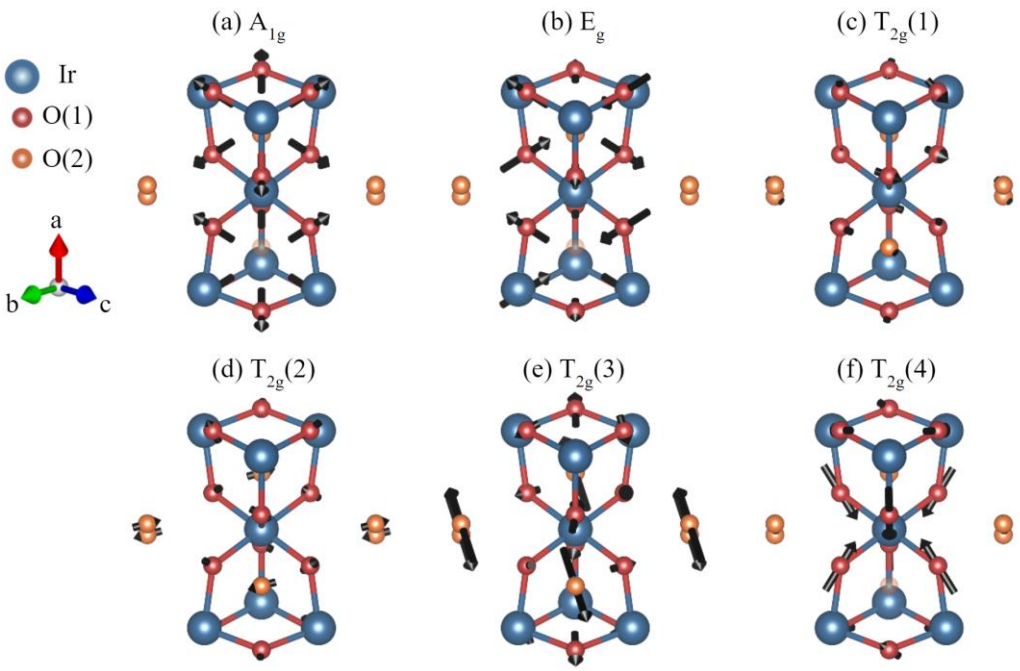

Figure 16. Atomic displacements of Raman active phonon modes in $Y_2Ir_2O_7$

follows a monotonic blueshift [blue solid lines in Fig. 17c] because of the thermal effect [72]. Below T_N, in contrast, the frequency of the A_{1g} mode significantly deviates from the thermal behavior and softens with decreasing T. Such T evolution implies strong SPC. The full width at half maximum of the A_{1g} mode also exhibits a kink at T_N, as shown in the inset of Fig. 17c. We define the peak shift $\Delta\omega$ (= $\omega_0 - \omega_{10K}$), where ω_0 is the constant obtained during the fitting process; experimental $\Delta\omega$ for the A_{1g} mode is ~2.3 ±0.3 cm^{-1}.

To extract the J and D values from the anomalous phonon softening, we calculated the J- and D-dependent $\Delta\omega$ using tight-binding calculations [61]. Our tight-binding calculations predict that the Dzyaloshinskii-Moriya interaction is the main contributor to phonon softening below T_N, consistent with the conclusion from the T dependence of IR-active phonons of $Y_2Ir_2O_7$ [61].

In general, the ion–ion interaction Hamiltonian H can be written as follows:

$$H = H_{\mathrm{latt}} + H_{\mathrm{spin}}. \tag{38}$$

Here, H_{latt} is associated with the lattice structure and the corresponding electrostatic potential of the ions, whereas H_{spin} is related to the spin structure of magnetic ions. For pyrochlore iridates, H_{spin} is given by

$$H_{\mathrm{spin}} = \sum_{ij}^{nn} J_{\mathrm{IE}_{ij}} \langle \mathbf{S}_i \cdot \mathbf{S}_j \rangle + \sum_{ij}^{nn} \mathbf{D}_{ij} \cdot \langle \mathbf{S}_i \times \mathbf{S}_j \rangle, \tag{39}$$

where $J_{\mathrm{IE}_{ij}}$ is the coefficient of the isotropic exchange interaction, D_{ij} ($\equiv \|\mathbf{D}_{ij}\|$) is the coefficient of the Dzyaloshinskii–Moriya (DM) interaction, and $\mathbf{S}_i$ is the pseudospin of the ith Ir ion. Here, we considered only the nearest-neighbor interactions by Σ_{ij}^{nn}. When spin-phonon coupling (SPC) turns on, the lattice vibration (or phonon) could be affected by spin ordering through H_{spin}, thereby inducing phonon renormalization of pyrochlore

iridates when the all-in-all-out magnetic (AIAO) ordering develops below T_N.

Vibrational motions of the pyrochlore lattice of $Y_2Ir_2O_7$ can cause variations in $J_{\mathrm{IE}_{ij}}$ and D_{ij} (i.e., $\Delta J_{\mathrm{IE}_{ij}}$ and $\Delta \mathrm{D}_{ij}$). We calculated the corresponding $\Delta J_{\mathrm{IE}_{ij}}$ and $\Delta \mathbf{D}_{ij}$ by Taylor series expansion up to the second-order term:

$$\Delta J_{\mathrm{IE}_{ij}}\big(\mathbf{u}_k(t)\big) \approx [\mathbf{u}_k(t)\cdot\nabla_k]J_{\mathrm{IE}_{ij}} + \tfrac{1}{2}[\mathbf{u}_k(t)\cdot\nabla_k]^2 J_{\mathrm{IE}_{ij}}, \tag{40}$$

$$\Delta \mathbf{D}_{ij}\big(\mathbf{u}_k(t)\big) \approx [\mathbf{u}_k(t)\cdot\nabla_k]\mathbf{D}_{ij} + \tfrac{1}{2}[\mathbf{u}_k(t)\cdot\nabla_k]^2 \mathbf{D}_{ij}, \tag{41}$$

where $\mathbf{u}_k(t)$ is the displacement vector from the equilibrium positions of the kth O ion placed between Ir ions, and ∇_k is a derivative operator. Here, the subscript k represents the kth O ion. The potential energy of the lattice vibration, U_{spin}, attributable to the H_{spin} term, is defined by

$$U_{\mathrm{spin}} = \frac{1}{2}\sum_{k,k',\alpha,\beta} \mathbf{u}_{k,\alpha}(t)\big[\mathbf{C}_{\mathrm{spin}}\big]_{k,k',\alpha,\beta}\mathbf{u}_{k',\beta}(t), \tag{42}$$

where $\mathbf{C}_{\mathrm{spin}}$ is the stiffness tensor, which can be written for pyrochlore iridates as

$$\big[\mathbf{C}_{\mathrm{spin}}\big]_{k,k',\alpha,\beta} = \frac{\partial^2 J_{\mathrm{IE}_{ij}}(\mathbf{u})}{\partial \mathbf{u}_{k,\alpha}\partial \mathbf{u}_{k',\beta}}\langle \mathbf{S}_i\cdot\mathbf{S}_j\rangle + \frac{\partial^2 \mathbf{D}_{ij}(\mathbf{u})}{\partial \mathbf{u}_{k,\alpha}\partial \mathbf{u}_{k',\beta}}\cdot\langle \mathbf{S}_i\times\mathbf{S}_j\rangle. \tag{43}$$

Here, we assume that the terms $\langle \mathbf{S}_i\cdot\mathbf{S}_j\rangle$ and $\langle \mathbf{S}_i\times\mathbf{S}_j\rangle$ are nearly independent of ionic displacement.

Then the equation of motion for the kth O ion will be

$$\dot{\mathrm{P}}_{k,\alpha} = -[\nabla_k U]_\alpha = [\mathbf{M}\ddot{\mathbf{u}}]_{k,\alpha}. \tag{44}$$

By adopting harmonic solutions (like sine and cosine functions), this equation of motion can be rewritten as follows

$$[\mathbf{M}\ddot{\mathbf{u}}]_{k,\alpha} = \sum_{k',\beta} \mathrm{M}_{k,\alpha}\delta_{kk'}\delta_{\alpha\beta}\cdot\omega^2\mathbf{u}_{k',\beta} = \sum_{k',\beta}[\mathbf{C}]_{k,k',\alpha,\beta}\mathbf{u}_{k',\beta}. \tag{45}$$

Here, $\mathbf{C}$ is the stiffness tensor of the pyrochlore lattice, which can be influenced by SPC. This yields two eigenvalue equations:

$$\omega_0^2 \mathbf{u}^T \mathbf{M} \mathbf{u} = \omega_0^2 = \mathbf{u}^T \mathbf{C} \mathbf{u} \quad \text{(with SPC)}, \tag{46}$$

$$\omega_0'^{\,2} \mathbf{u}^T \mathbf{M} \mathbf{u} = \omega_0'^{\,2} = \mathbf{u}^T \mathbf{C}' \mathbf{u} \quad \text{(without SPC)}, \tag{47}$$

where ω_0 and ω_0' are dressed and bare phonon frequencies, and C and C' are stiffness tensors with and without the influence of SPC, respectively. Direct subtraction of (S22) from (S21) gives the phonon frequency shift, $\Delta\omega_0 = \omega_0 - \omega_0'$, due to SPC under coordinate transformation with $\mathbf{u} = \mathbf{M}^{-\frac{1}{2}} \hat{\mathbf{u}}$:

$$\Delta\omega_0 = \frac{1}{2\mu\omega} \hat{\mathbf{u}}^T \mathbf{C}_{\text{spin}} \hat{\mathbf{u}}, \tag{48}$$

where μ is the reduced mass of *n* harmonic oscillators.

Finally, we obtain $\Delta\omega_0$ by substituting $\mathbf{C}_{\text{spin}}$ in (43) into (48):

$$\Delta\omega_0 = \frac{1}{2\mu\omega_0} \sum_k \{[\hat{\mathbf{u}}_k(t) \cdot \nabla_k]^2 J_{\text{IE}_{ij}} \langle \mathbf{S}_i \cdot \mathbf{S}_j \rangle + [\hat{\mathbf{u}}_k(t) \cdot \nabla_k]^2 \mathbf{D}_{ij} \cdot \langle \mathbf{S}_i \times \mathbf{S}_j \rangle\}. \tag{49}$$

Phonon renormalization in the pyrochlore iridate system is primarily attributable to changes in the Ir-O-Ir bond angle θ; thus, we can transform equation (49) from Cartesian to cylindrical coordinates, as follows

$$\hat{\mathbf{u}}_k(t) \cdot \nabla_k \approx \frac{1}{l}\left(\frac{\partial}{\partial\alpha}\right) = -\frac{2}{l}\left(\frac{\partial}{\partial\theta}\right) \quad (\theta = \pi - 2\alpha), \tag{50}$$

where *l* is the Ir-O bond length.

Hence, the phonon frequency shift $\Delta\omega_0$ in (50) can be written as a function of θ:

$$\Delta\omega_0 = \frac{2}{I\omega}\left(\sum_{i,j}^{\text{nn}} \frac{\partial^2 J_{\text{IE}_{ij}}(\theta)}{\partial\theta^2} \langle \mathbf{S}_i \cdot \mathbf{S}_j \rangle + \sum_{i,j}^{\text{nn}} \frac{\partial^2 \vec{D}_{ij}(\theta)}{\partial\theta^2} \cdot \langle \mathbf{S}_i \times \mathbf{S}_j \rangle\right), \tag{51}$$

where the rotational moment of inertia is defined as $I \equiv \mu l^2$.

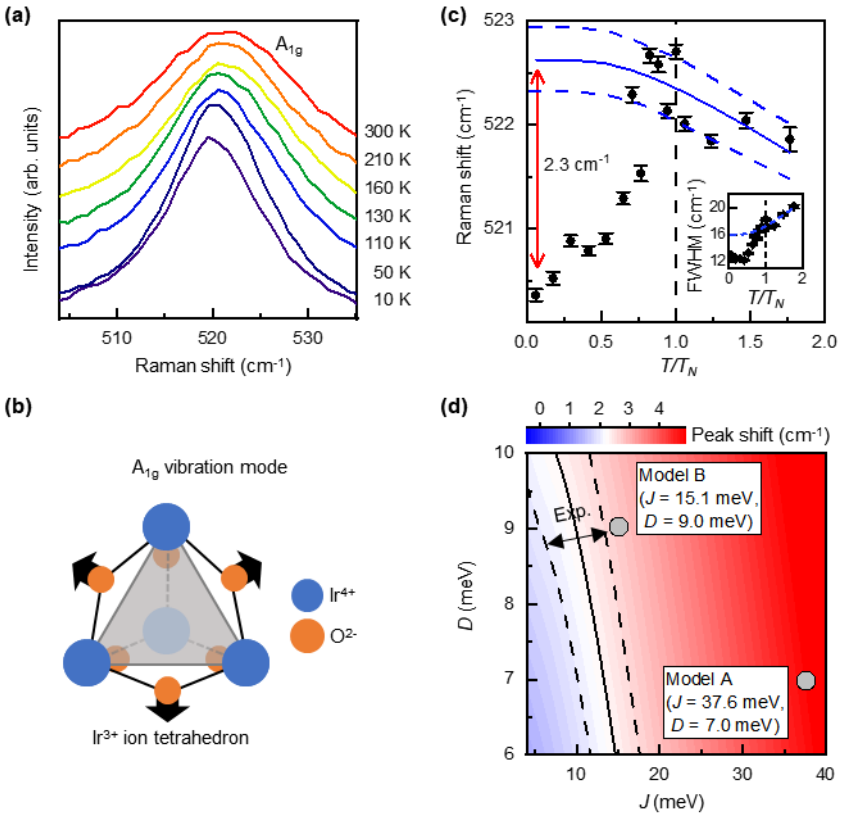

Figure 17. a T evolution of the A_{1g} phonon. b Atomic displacement of the A_{1g} phonon of $Y_2Ir_2O_7$. c T-dependence of the phonon shift (black circles) and the full width at half maximum (FWHM, black squares in inset) of the A_{1g} phonon obtained by Lorentzian fitting. Blue solid and dashed lines are the anharmonic fitting curves for the T-dependence of the phonon shift and linewidth, respectively. Thermal fluctuations of the peak shift around T_N indicate that the fitting curve for the peak shift in c is not unique, leading to a shift of the A_{1g} phonon of approximately $\Delta\omega = 2.3 \pm 0.3$ cm^{-1}. d Contour map of the phonon shift calculated for J and D values. The peak shift is indicated by color-coding. Solid and dashed lines indicate the experimental values of the peak shift and error bars: $\Delta\omega = 2.3 \pm 0.3$ cm^{-1}. Gray circles represent the calculated peak shifts corresponding to the J and D parameters of Models A and B.

Figure 17d shows a contour plot of the calculated peak shift $\Delta\omega$ of the A_{1g} phonon mode for various J and D values. The solid line and two dashed lines display the J and D values, which can produce the peak shift with error bars: $\Delta\omega = 2.3 \pm 0.3$ cm^{-1}. The gray circles

indicate the J and D values obtained from equations (27) and (28) for Models A and B. Importantly, only Model B (i.e., J = 15.1 and D = 9.0 meV) can explain the experimental phonon shift. The calculated $\Delta\omega$ values from Models B and A are approximately 2.6 $cm^{-1}$and 5.0 cm^{-1}, respectively. Therefore, we concluded that the MB dispersion of $Y_2Ir_2O_7$ can be described by Model B with c-MB topology.

4.5 Conclusion

Through a combined Raman spectroscopy and tight-binding calculation study, we showed that $Y_2Ir_2O_7$ hosts the crossing magnon band topology. The analyses on the resonance energies of the single magnon excitations and the anomalous phonon softening in the antiferromagnetic phase led to a unique determination of the magnetic interaction parameters of $R_2Ir_2O_7$. The values of the magnetic interaction parameters from our analyses

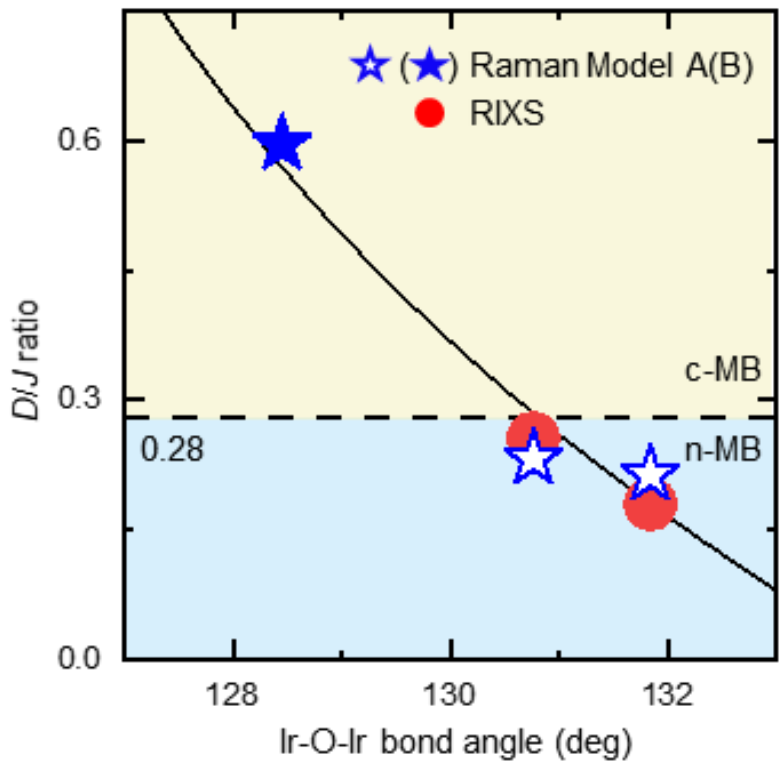

Figure 18. Ir-O-Ir bond-angle (θ) dependence of J/D obtained from tight-binding calculations on $R_2Ir_2O_7$ (R: Sm, Eu, Y). Our results indicate that $Y_2Ir_2O_7$ is the only candidate in the $Y_2Ir_2O_7$ system to have c-MB topology.

indicate that $Y_2Ir_2O_7$ has the crossing magnon band and $Sm_2Ir_2O_7$/$Eu_2Ir_2O_7$ shows noncrossing magnon band. The distinct magnon band topologies are expected to manifest themselves in the thermal Hall effect. It is worth performing magnon thermal Hall measurements to confirm the rich phases of the nontrivially topological properties $R_2Ir_2O_7$. Our result indicates that the pyrochlore iridates R_2IrO_7 is a unique system where the magnon band topology can be tuned, which has been challenging in topological electronic systems. Our study also suggests that Raman spectroscopy is a simple and powerful tool to investigate magnon excitations and spin Hamiltonian of the AIAO 5*d* pyrochlore iridate $R_2Ir_2O_7$.

Chapter 5

Summary and Concluding Remarks

To summarize, we investigated the effect of strong spin-orbit coupling on the 5d pyrochlore iridates using various optical spectroscopic technique.

First, we provided the unconventional spin-phonon coupling mechanism via Dzyaloshinskii-Moriya (DM) interaction. Infrared-active phonon spectra shows the phonon renormalization phenomena near the transition temperature T_N. Using the density functional calculation and tight-binding model analysis, we found that DM interactions is the main contributor of this spin-phonon coupling.

Second, our study enriches the magnon topological phase diagram of pyrochlore iridate system. Using the Raman spectroscopy, we observed the magnetic excitation peak for three pyrochlore iridate materials below the transition temperature T_N. Previous Raman study and RIXS studies already provide the evidence of single-magnon excitation. Providing the single-magnon mechanism for pseudospin states, we suggest that pyrochlore iridate system can show the single-magnon scattering signal on their Raman spectra. Also, there are two possible spin Hamiltonian models (Model A and B) for $Y_2Ir_2O_7$. Using the tight-binding model analysis, we identify that Model B is the suitable model for $Y_2Ir_2O_7$. It means that $Y_2Ir_2O_7$ has different topological magnon state from the other pyrochlore iridate materials.

This result corrects the insight of pyrochlore iridate system and reinforce the importance of strong SOC effect in the 5*d* TMO.

Chapter 6

References

Bibliography

[1] B. J. Kim, H. Jin, S. J. Moon, J.-Y. Kim, B.-G. Park, C. S. Leem, J. Yu, T. W. Noh, C. Kim, S.-J. Oh, J.-H. Park, V. Durairaj, G. Cao, and E. Rotenberg, Phys. Rev. Lett. **101**, 076402 (2008).

[2] X.-L. Qi and S.-C. Zhang, Rev. Mod. Phys. **83**, 1057 (2011).

[3] M. Z. Hasan and C. L. Kane, Rev. Mod. Phys. **82**, 3045 (2010).

[4] N. P. Armitage, E. J. Mele, and A. Vishwanath, Rev. Mod. Phys. **90**, (2018).

[5] X. Wan, A. M. Turner, A. Vishwanath, and S. Y. Savrasov, Phys. Rev. B - Condens. Matter Mater. Phys. **83**, 205101 (2011).

[6] Y. Wang, H. Weng, L. Fu, and X. Dai, Phys. Rev. Lett. **119**, 187203 (2017).

[7] K. Ueda, J. Fujioka, and Y. Tokura, Phys. Rev. B **93**, 1 (2016).

[8] Y. Machida, S. Nakatsuji, S. Onoda, T. Tayama, and T. Sakakibara, Nature **463**, 210 (2010).

[9] W. Witczak-Krempa and Y. B. Kim, Phys. Rev. B - Condens. Matter Mater. Phys. **85**, 045124 (2012).

[10] C. H. Sohn, C. H. Kim, L. J. Sandilands, N. T. M. Hien, S. Y. Kim, H. J. Park, K. W. Kim, S. J. Moon, J. Yamaura, Z. Hiroi, and T. W. Noh, Phys. Rev. Lett. **118**, 117201 (2017).

[11] T. M. H. Nguyen, L. J. Sandilands, C. H. Sohn, C. H. Kim, A. L. Wysocki, I. S. Yang, S. J. Moon, J. H. Ko, J. Yamaura, Z. Hiroi, and T. W. Noh, Nat. Commun. **8**, 251 (2017).

[12] D. Pesin and L. Balents, Nat. Phys. **6**, 376 (2010).

[13] T. Moriya, Phys. Rev. **120**, 91 (1960).

[14] H. Jin, H. Jeong, T. Ozaki, and J. Yu, Phys. Rev. B **80**, 075112 (2009).

[15] C. Kittel and U. C. Kittel, *Introduction to Solid State Physics* (Wiley, 1971).

[16] S. Lee, A. Pirogov, M. Kang, K.-H. Jang, M. Yonemura, T. Kamiyama, S.-W. Cheong, F. Gozzo, N. Shin, H. Kimura, Y. Noda, and J.-G. Park, Nature **451**, 805 (2008).

[17] J. Laverdière, S. Jandl, A. A. Mukhin, V. Y. Ivanov, V. G. Ivanov, and M. N. Iliev, Phys. Rev. B **73**, 214301 (2006).

[18] J. S. Lee, T. W. Noh, J. S. Bae, I. S. Yang, T. Takeda, and R. Kanno, Phys. Rev. B - Condens. Matter Mater. Phys. **69**, (2004).

[19] H. J. Silverstein, K. Fritsch, F. Flicker, A. M. Hallas, J. S. Gardner, Y. Qiu, G. Ehlers, A. T. Savici, Z. Yamani, K. A. Ross, B. D. Gaulin, M. J. P. Gingras, J. A. M. Paddison, K. Foyevtsova, R. Valenti, F. Hawthorne, C. R. Wiebe, and H. D. Zhou, Phys. Rev. B **89**, 054433 (2014).

[20] E. Granado, N. O. Moreno, H. Martinho, A. García, J. A. Sanjurjo, I. Torriani, C. Rettori, J. J. Neumeier, and S. B. Oseroff, Phys. Rev. Lett. **86**, 5385 (2001).

[21] S. Issing, A. Pimenov, V. Y. Ivanov, A. A. Mukhin, and J. Geurts, Phys. Rev. B **81**, 24304 (2010).

[22] D. A. Mota, Y. Romaguera Barcelay, P. B. Tavares, M. R. Chaves, A. Almeida, J. Oliveira, W. S. Ferreira, and J. Agostinho Moreira, J. Phys. Condens. Matter **25**, 235602 (2013).

[23] S. Petit, F. Moussa, M. Hennion, S. Pailhès, L. Pinsard-Gaudart, and A. Ivanov, Phys. Rev. Lett. **99**, 266604 (2007).

[24] S. Lee, S. Onoda, and L. Balents, Phys. Rev. B - Condens. Matter Mater. Phys. **86**, 1 (2012).

[25] A. B. Sushkov, O. Tchernyshyov, W. R. II, S. W. Cheong, and H. D. Drew, Phys. Rev. Lett. **94**, 137202 (2005).

[26] S. Bordács, D. Varjas, I. Kézsmárki, G. Mihály, L. Baldassarre, A. Abouelsayed, C. A. Kuntscher, K. Ohgushi, and Y. Tokura, Phys. Rev. Lett. **103**, 77205 (2009).

[27] C. Kant, J. Deisenhofer, T. Rudolf, F. Mayr, F. Schrettle, A. Loidl, V. Gnezdilov, D.

Wulferding, P. Lemmens, and V. Tsurkan, Phys. Rev. B **80**, 214417 (2009).

[28] H. Sakai, J. Fujioka, T. Fukuda, M. S. Bahramy, D. Okuyama, R. Arita, T. Arima, A. Q. R. Baron, Y. Taguchi, and Y. Tokura, Phys. Rev. B **86**, 104407 (2012).

[29] S. W. Cheong and M. Mostovoy, Nat. Mater. **6**, 13 (2007).

[30] M. Fiebig, T. Lottermoser, D. Meier, and M. Trassin, Nat. Rev. Mater. **1**, 16046 (2016).

[31] K. V Shanavas, Z. S. Popović, and S. Satpathy, Phys. Rev. B **90**, 165108 (2014).

[32] S. M. Disseler, Phys. Rev. B - Condens. Matter Mater. Phys. **89**, 140413(R) (2014).

[33] T. H. Arima, J. Phys. Soc. Japan **82**, 1 (2013).

[34] C. C. Homes, M. Reedyk, D. A. Cradles, and T. Timusk, Appl. Opt. **32**, 2976 (2009).

[35] L. J. P. Ament, G. Khaliullin, and J. Van Den Brink, Phys. Rev. B - Condens. Matter Mater. Phys. **84**, 2 (2011).

[36] S. Kumar and H. C. Gupta, Vib. Spectrosc. **62**, 180 (2012).

[37] N. T. Vandenexorre and E. H. H. Brusset, **37**, 113 (1981).

[38] J. Menéndez and M. Cardona, Phys. Rev. B **29**, 2051 (1984).

[39] J. S. Lee, T. W. Noh, J. S. Bae, I.-S. Yang, T. Takeda, and R. Kanno, Phys. Rev. B **69**, 214428 (2004).

[40] M. C. Shapiro, S. C. Riggs, M. B. Stone, C. R. De La Cruz, S. Chi, A. A. Podlesnyak, and I. R. Fisher, Phys. Rev. B - Condens. Matter Mater. Phys. **85**, 214434 (2012).

[41] J. P. Clancy, H. Gretarsson, E. K. H. Lee, D. Tian, J. Kim, M. H. Upton, D. Casa, T. Gog, Z. Islam, B. G. Jeon, K. H. Kim, S. Desgreniers, Y. B. Kim, S. J. Julian, and Y. J. Kim, Phys. Rev. B **94**, 024408 (2016).

[42] H. Takatsu, K. Watanabe, K. Goto, and H. Kadowaki, Phys. Rev. B **90**, 235110 (2014).

[43] G. Kresse and J. Hafner, Phys. Rev. B **48**, 13115 (1993).

[44] H. Kumar and A. K. Pramanik, AIP Conf. Proc. **1731**, 130053 (2016).

[45] W. A. Harrison, *Electronic Structure and the Properties of Solids: The Physics of*

the Chemical Bond (Courier Corporation, New York, 1989).

[46] J. C. Slater and G. F. Koster, Phys. Rev. **94**, 1498 (1954).

[47] R. Yadav, M. Pereiro, N. A. Bogdanov, S. Nishimoto, A. Bergman, O. Eriksson, J. Van Den Brink, and L. Hozoi, Phys. Rev. Mater. **2**, 74408 (2018).

[48] C.-K. Chiu, J. C. Y. Teo, A. P. Schnyder, and S. Ryu, Rev. Mod. Phys. **88**, 35005 (2016).

[49] F.-Y. Li, Y.-D. Li, Y. B. Kim, L. Balents, Y. Yu, and G. Chen, Nat. Commun. **7**, 12691 (2016).

[50] A. Mook, J. Henk, and I. Mertig, Phys. Rev. Lett. **117**, 157204 (2016).

[51] K. Li, C. Li, J. Hu, Y. Li, and C. Fang, Phys. Rev. Lett. **119**, 247202 (2017).

[52] W. Yao, C. Li, L. Wang, S. Xue, Y. Dan, K. Iida, K. Kamazawa, K. Li, C. Fang, and Y. Li, Nat. Phys. **14**, 1011 (2018).

[53] K. Hwang, N. Trivedi, and M. Randeria, Phys. Rev. Lett. **125**, 047203 (2020).

[54] C. Donnerer, M. C. Rahn, M. M. Sala, J. G. Vale, D. Pincini, J. Strempfer, M. Krisch, D. Prabhakaran, A. T. Boothroyd, and D. F. McMorrow, Phys. Rev. Lett. **117**, 037201 (2016).

[55] C. Donnerer, X-Ray Studies of Magnetic and Structural Transitions in Iridates, University College London, 2017.

[56] S. H. Chun, B. Yuan, D. Casa, J. Kim, C. Y. Kim, Z. Tian, Y. Qiu, S. Nakatsuji, and Y. J. Kim, Phys. Rev. Lett. **120**, 177203 (2018).

[57] Q. Yan, R. Liu, Z. Yan, B. Liu, H. Chen, Z. Wang, and L. Lu, Nat. Phys. **14**, 461 (2018).

[58] S. M. Souliou, J. Chaloupka, G. Khaliullin, G. Ryu, A. Jain, B. J. Kim, M. Le Tacon, and B. Keimer, Phys. Rev. Lett. **119**, 067201 (2017).

[59] H. Gretarsson, N. H. Sung, M. Höppner, B. J. Kim, B. Keimer, and M. Le Tacon, Phys. Rev. Lett. **116**, 136401 (2016).

[60] Y. Tian, A. A. Reijnders, G. B. Osterhoudt, I. Valmianski, J. G. Ramirez, C. Urban, R. Zhong, J. Schneeloch, G. Gu, I. Henslee, and K. S. Burch, Rev. Sci. Instrum. **87**, 43105 (2016).

[61] J. Son, B. C. Park, C. H. Kim, H. Cho, S. Y. Kim, L. J. Sandilands, C. Sohn, J.-G. Park, S. J. Moon, and T. W. Noh, Npj Quantum Mater. **4**, 17 (2019).

[62] K. Ueda, R. Kaneko, A. Subedi, M. Minola, B. J. Kim, J. Fujioka, Y. Tokura, and B. Keimer, Phys. Rev. B **100**, 115157 (2019).

[63] T. Hasegawa, N. Ogita, K. Matsuhira, S. Takagi, M. Wakeshima, Y. Hinatsu, and M. Udagawa, J. Phys. Conf. Ser. **200**, (2010).

[64] Z. Hiroi, J. Yamaura, T. Hirose, I. Nagashima, and Y. Okamoto, APL Mater. **3**, 41501 (2015).

[65] L. Hozoi, H. Gretarsson, J. P. Clancy, B. G. Jeon, B. Lee, K. H. Kim, V. Yushankhai, P. Fulde, D. Casa, T. Gog, J. Kim, A. H. Said, M. H. Upton, Y. J. Kim, and J. Van Den Brink, Phys. Rev. B - Condens. Matter Mater. Phys. **89**, 1 (2014).

[66] P. A. Fleury and R. Loudon, Phys. Rev. **166**, 514 (1968).

[67] N. Taira, M. Wakeshima, and Y. Hinatsu, J. Phys. Condens. Matter **11**, 6983 (1999).

[68] H. Guo, C. Ritter, and A. C. Komarek, Phys. Rev. B **94**, 1 (2016).

[69] E. Lefrançois, V. Simonet, R. Ballou, E. Lhotel, A. Hadj-Azzem, S. Kodjikian, P. Lejay, P. Manuel, D. Khalyavin, and L. C. Chapon, Phys. Rev. Lett. **114**, 1 (2015).

[70] R. J. Elliott and R. Loudon, Phys. Lett. **3**, 189 (1963).

[71] A. P. Cracknell, J. Phys. C Solid State Phys. **2**, 500 (1969).

[72] M. Balkanski, R. F. Wallis, and E. Haro, Phys. Rev. B **28**, 1928 (1983).

Chapter 7
Appendix

7.1 Regime III of the magnon dispersion for $R_2Ir_2O_7$

In Ref. [53], it is predicted that a topological phase transition of magnon band from regime II to regime III occurs at $D/J > 1/\sqrt{2} \cong 0.71$; another magnon band inversion appears at the X point. In the calculations of Ref. [53], the anisotropic exchange interaction term $\mathbb{A}$ is not included. In fact, the inclusion of the $\mathbb{A}$ term at $D/J > 0.71$ prevents magnon band inversion at point X; regime III cannot be realized, as detailed below.

With the the $\mathbb{A}$ term, the phase boundary between regime II and regime III can be redefined by replacing J with $J' = (J + 2\mathbb{A})$ and D with $D' = \left(D - \frac{3\sqrt{2}}{4}\mathbb{A}\right)$. The condition for regime III then changes as follows:

$$\frac{D'}{J'} = \frac{\left(D - \frac{3\sqrt{2}}{4}\mathbb{A}\right)}{(J + 2\mathbb{A})} > \frac{1}{\sqrt{2}}. \tag{52}$$

We plot the D'/J' ratio as a function of D/J in Fig. 19. It is clear that D'/J' cannot exceed $1/\sqrt{2} \cong 0.71$ over a wide range of values for the D/J ratio (we allow the D/J ratio to vary between 0 and 5 in our calculations; in the real materials R227, the range would be much smaller). This means that, when the $\mathbb{A}$ term is included, the ratio between the DM and Heisenberg interactions cannot fall into that of regime III.

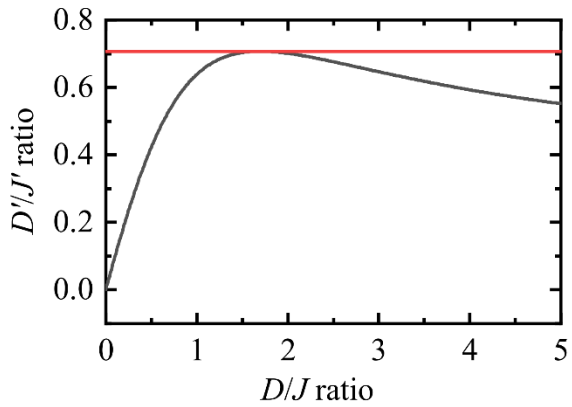

Figure 19. Variation of the D'/J' ratio as a function of the D/J ratio. The black curve is the D'/J' curve and the red solid line has a value of 0.71, which is the phase boundary between regimes II ($D'/J' < 0.71$) and III ($D'/J' > 0.71$). The D'/J' curve does not exceed 0.71, implying that regime III cannot exist when the $\mathbb{A}$ term is included.

7.2 Laser dependence of the M_1 and M_2 peaks

We checked the laser dependence of the M_1 and M_2 excitations using 671- and 532-nm excitation sources. As shown in Fig. 20, at 10 K, the energies of M_1 and M_2 are unchanged under the irradiation at either 671 or 532 nm. This confirms that M_1 and M_2 are indeed Raman excitations, and not photoluminescence. At 200 K, both M_1 and M_2 are almost completely suppressed. The slight difference in phonon frequency of the $T_{2g}(2)$ mode between the two lasers, which were operating at the same temperature may reflect imperfect calibration. The 532-nm laser was used in the temperature dependence experiment because it exhibited a better signal-to-noise ratio than the 671-nm laser.

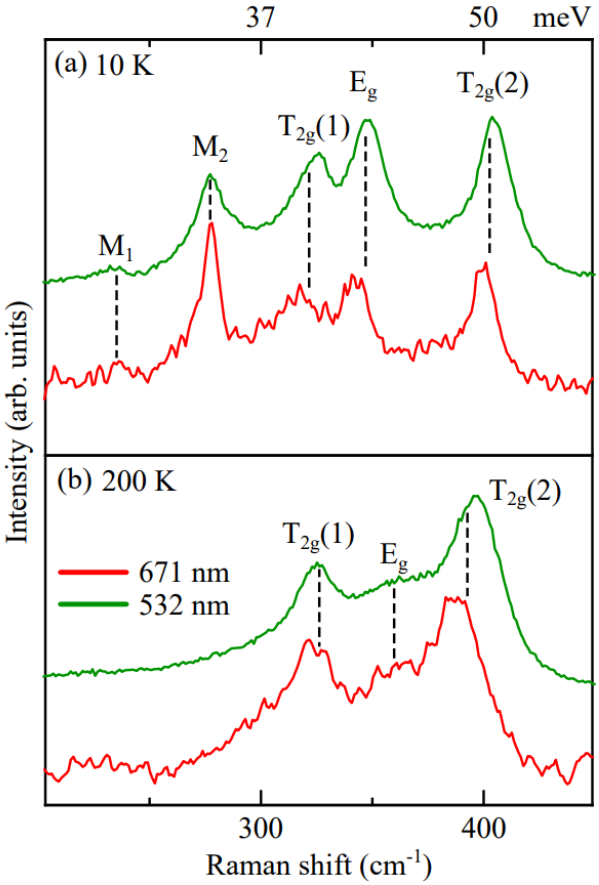

Figure 20. Raman spectra of $Y_2Ir_2O_7$ at 10 K (upper panel) and 200 K (lower panel) were measured using a 532-nm laser (green line) and a 671-nm laser (red line).

7.3 Magnetic point group analysis for AIAO pyrochlore iridate $Y_2Ir_2O_7$

To establish irreducible co-representations of the Raman tensors for $Y_2Ir_2O_7$ (or general $A_2B_2O_7$), it is necessary to know its magnetic point group in both the paramagnetic and antiferromagnetic phases. We used the method presented in Ref. [70] to derive the magnetic point group of $Y_2Ir_2O_7$.

The crystal structure of $R_2Ir_2O_7$ is cubic with and *Fd-3m* space group (O_h group) and

there is no structure transition across the magnetic phase transition. Therefore, in the paramagnetic phase ($T>T_N$) there are 48 allowed symmetry operations of the O_h group:

$$\mathbf{G}= 1,\ \bar{1}, 9(2),\ 9\,(\bar{2}),\ 4(\pm 3),\ 4(\pm\bar{3}),\ 3(\pm 4),\ 3(\pm\bar{4}), \qquad (52)$$

where all operations have their usual meaning: 1=identity; $\bar{1}$= inversion through the symmetry center; m(n)=number of rotation axes C_n, e.g., 9(2) means 9 C_2; ± represent the clockwise or anticlockwise direction of rotation of C_n; and $\bar{n}$ corresponds to a reflection with a mirror perpendicular to C_n.

In the antiferromagnetic phase, $T<T_N$, there are 24 remaining (unchanged) *unitary* symmetry operations:

$$\mathbf{H}= 1,\ \bar{1},\ 3(2), 3(\bar{2}), 4(\pm 3), 4(\pm\bar{3}). \qquad (53)$$

Therefore, the G−H unitary operations that are not allowed below T_N are:

$$(\mathbf{G}-\mathbf{H}) = 6(2),\ 6\,(\bar{2}), 3(\pm 4), 3(\pm\bar{4}). \qquad (54)$$

Combining **G−H** with the time-reversal operation θ, forms *antiunitary* operations θ (**G−H**) (represented in what follows by an underline); then

$$\theta(\mathbf{G}-\mathbf{H})= 6(\underline{2}),\ 6\,(\underline{\bar{2}}), 3(\pm\underline{4}), 3(\pm\underline{\bar{4}}). \qquad (55)$$

The allowed unitary+antiunitary operations for $Y_2Ir_2O_7$ below T_N are:

$$\mathbf{M}= \mathbf{H}+\theta(\mathbf{G}\text{-}\mathbf{H}) =1,\ \bar{1}, 3(2),\ 3\,(\bar{2}),\ 4(\pm 3),\ 4(\pm\bar{3}),\ 6(\underline{2}),\ 6\,(\underline{\bar{2}}), 3(\pm\underline{4}), 3(\pm\underline{\bar{4}}) \qquad (56)$$

According to Ref. [71] the magnetic point group for $Y_2Ir_2O_7$ is ($m3m'$).

Table 4. Raman tensors for the magnetic point group $m3m'$.

$m3m'$	Symmetry A_g	E_g	E_g	T_g
Tensor representation	$\begin{pmatrix} A & 0 & 0 \\ 0 & A & 0 \\ 0 & 0 & A \end{pmatrix}$	$\begin{pmatrix} \omega^* B & 0 & 0 \\ 0 & \omega B & 0 \\ 0 & 0 & B \end{pmatrix}$	$\begin{pmatrix} \omega C & 0 & 0 \\ 0 & \omega^* C & 0 \\ 0 & 0 & C \end{pmatrix}$	$\left\langle \begin{pmatrix} 0 & 0 & 0 \\ 0 & 0 & iF \\ 0 & -iF & 0 \end{pmatrix} \begin{pmatrix} 0 & 0 & -iF \\ 0 & 0 & 0 \\ iF & 0 & 0 \end{pmatrix} \begin{pmatrix} 0 & iF & 0 \\ -iF & 0 & 0 \\ 0 & 0 & 0 \end{pmatrix} \right\rangle$

[1] A, B, C, and F are real.
[2] $\omega = \exp(2\pi i/3)$

Chapter 8

Publication list

1. Thi Huyen Nguyen, **Jaeseok Son**, Soyeun Kim, Hwanbeom Cho, Choong H. Kim, Yiping Wang, Kenneth S. Burch, In-Sang Yang, Jaehong Jeong, Je-Geun Park, Soon Jae Moon, and Tae Won Noh, *Topological Magnon Band Crossing in* $Y_2Ir_2O_7$, under review in Phys. Rev. Lett (2021).
2. Yangyang Li, Taekoo Oh, **Jaeseok Son**, Jeongkeun Song, Mi Kyung Kim, Dongjun Song, Sukhyun Kim, Seo Hyoung Chang, Changyoung Kim, Bohm-Jung Yang, and Tae Won Noh, *Correlated Magnetic Weyl Semimetal State in Strained* $Pr_2Ir_2O_7$, Adv. Mater. 2008528 (2021).
3. Woo Jin Kim, Taekoo Oh, Jeongkeun Song, Eun Kyo Ko, Yangyang Li, Junsik Mun, Bongju Kim, **Jaeseok Son**, Zhuo Yang, Yoshimitsu Kohama, Miyoung Kim, Bohm-Jung Yang and Tae Won Noh, *Strain engineering of the magnetic multipole moments and anomalous Hall effect in pyrochlore iridate thin films*, Sci. Adv. **6**, 29 (2020).
4. Songhee Choi, Joongoo Kang, Sangkyun Ryu, Hyoungjeen Jeen, **Jaeseok Son**, and Shinbuhm Lee, *High infrared transparency up to 8-μm-wavelength in correlated vanadium Wadsley conductors*, APL Mater. **8**, 041111 (2020).
5. Seung Gyo Jeong, Taewon Min, Sungmin Woo, Jiwoong Kim, Yu-Qiao Zhang, Seong Won Cho, **Jaeseok Son**, Young-Min Kim, Jung Hoon Han, Sungkyun Park, Hu Young Jeong, Hiromichi Ohta, Suyoun Lee, Tae Won Noh, Jaekwang Lee, Woo Seok Choi, *Phase instability amid dimensional crossover in artificial oxide crystal*, Phys. Rev.

Lett. **124**, 026401 (2020).

6. Songhee Choi, **Jaeseok Son**, Junhyeob Oh, Ji-Hyun Lee, Jae Hyuck Jang, and Shin-buhm Lee, *Sharp contrast in the electrical and optical properties of vanadium Wadsley (V_mO_{2m+1}, m>1) epitaxial films selectively stabilized on (111)-oriented Y-stabilized ZrO_2*, Phys. Rev. Mater. **3**, 063401 (2019).
7. **Jaeseok Son**, Byung Cheol Park, Choong H. Kim, Hwanbeom Cho, So Yeun Kim, Luke J. Sandilands, Changhee Sohn, Je-Geun Park, Soon Jae Moon & Tae Won Noh, *Unconventional spin-phonon coupling via the Dzyaloshinskii–Moriya interaction*, npj Quantum Mater. **4**, 17 (2019).
8. So Yeun Kim, Tae Yun Kim, Luke J. Sandilands, Soobin Sinn, Min-Cheol Lee, **Jaeseok Son**, Sungmin Lee, Ki-Young Choi, Wondong Kim, Byeong-Gyu Park, C. Jeon, Hyeong-Do Kim, Cheol-Hwan Park, Je-Geun Park, S. J. Moon, and T. W. Noh, *Charge-Spin Correlation in van der Waals Antiferromagnet $NiPS_3$*, Phys. Rev. Lett. **120**, 136402 (2018).
9. Luke J. Sandilands, Wonshik Kyung, So Yeun Kim, **Jaeseok Son**, J. Kwon, Tae Dong Kang, Y. Yoshida, Soon Jae Moon, C. Kim, and Tae Won Noh, *Spin-Orbit Coupling and Interband Transitions in the Optical Conductivity of Sr_2RhO_4*, Phys. Rev. Lett. **119**, 267402 (2017).

Chapter 9

Korean Abstract

국문초록

파이로클로로 이리듐 산화물에서의 자기적 들뜸 현상에 대한 분광학 연구

본 학위 논문에서는 파이로클로로 이리듐 산화물의 비평행 자기정렬 구조에서 나타날 수 있는 물리적 현상에 대한 연구를 진행하였습니다. 파이로클로로 정사면체 격자 구조와 강한 스핀-궤도 결합이 공존하는 파이로클로로 이리듐 산화물 시스템은 소위 올인-올아웃 (All-in-All-Out) 정렬이라는 특이한 비평행 자기정렬 구조를 보여줍니다. 이러한 독특한 자기 구조를 바탕으로, 파이로클로로 이리듐 산화물 시스템에 새로운 스핀-포논(spin-phonon) 결합과 마그논(magnon)의 특별한 위상학적 상태가 발현될 수 있습니다. 본 연구에서는 다양한 광학 분광 기법을 사용하여 이러한 현상의 기작을 밝히고, 5d 전이 금속 산화물 시스템에 대한 물리학에 대한 이해를 도모합니다.

이리듐 산화물의 경우 비슷한 규모의 전자간 쿨롱 상호작용(U)과 강한 스핀-궤도 결합 상호작용은 상대론적 모트(Mott) 절연체 상태를 (J_{eff}=1/2 전자 기저상태) 유도합니다. 파이로클로로 격자 구조는 그들의 강한 SOC로 인해 자기 이온 간의 비등방성 교환 상호작용이 강화됩니다. 이러한 상호작용은 자기적 불안정성을 감소시키고, 비평행 올인-올아웃 자성을 유도하는 데 중요한 역할을 합니다. 이러한 종류의 교환 상호작용은 가장 가까운 이온 사이를 매개하는 산소 이온에 의해 조절될 수 있습니다.

결론적으로, 이것이 산소 이온의 진동에 영향을 받는 포논 모드가 스핀 구조와 결합되는 이유입니다. 이러한 측면에서 5d 전이금속 산화물에서 보고되지 않은 않은 스핀-포논 결합 현상을 조사할 필요성이 있습니다.

첫 번째 주제는 $Y_2Ir_2O_7$에서 잘로진스키-모리야(Dzyaloshinskii-Moriya; DM) 상호작용을 통한 새로운 스핀-포논 결합 현상입니다. 3d 전이금속 산화물에서 하이젠베르크(Heisenberg) 교환 상호작용은 스핀-포논 결합 동작의 주요 원인입니다. 여기서는 스핀-궤도 결합이 약하기 때문에 이로 의해 매개되는 비등방성 교환 상호작용이 매우 억제됩니다. 그러나 5d 전이금속 산화물에서는 강한 스핀-궤도 결합이 비등방성 교환 상호작용을 증폭시켜 하이젠베르크 교환 상호작용과 견줄 만한 규모로 커질 수 있습니다. 푸리에 변환 적외선 분광기법으로 측정한 $Y_2Ir_2O_7$ 의 광학 포논 스펙트럼에서 온도에 따른 급격한 포논 재정규화 현상을 발견했습니다. 밀도 함수 이론(DFT) 계산을 바탕으로, 포논 재정규화는 Ir-O-Ir 벤딩 모드를 통한 자기 교환 상호작용의 변화에서 비롯된다는 것을 알 수 있습니다. 타이트-바인딩(tight-binding) 모형 분석을 사용하여 DM 상호작용이 $Y_2Ir_2O_7$의 포논 재규격화의 주요 원인임을 밝혀냈습니다. 이 결과는 강한 스핀-궤도 결합이 5d 전이금속 산화물 및 비평형 자기 구조 물질에서 스핀-포논 결합에 중요한 역할을 한다는 것을 나타냅니다.

두 번째로, 우리는 파이로클로로 이리듐 산화물의 마그논의 위상학적 상태와 그것들 사이의 위상전이 현상을 라만 분광학을 통해 연구하였습니다. DM 상호작용과 하이젠베르크 상호작용 사이의 비율은 파이로클로로 이리듐 산화물 시스템에서 마그논 위상을 결정하는 요소로 알려져 있습니다. 이리듐 산화물에서 자기 구조 측정에 대한 실험적인 어려움 때문에, 파이로클로로 이리듐 산화물 연구에서 기존의 실험 방법으로 마그논의

위상학적 특성을 확인하는 것은 어렵습니다. 본 연구에서는 라만 분광기를 이용하여 이러한 어려움을 극복하고, 고해상도로 $R_2Ir_2O_7$(R:Y, Eu, Sm)의 자기적 신호를 측정하였습니다. $Eu_2Ir_2O_7$ 및 $Sm_2Ir_2O_7$에 대한 이전의 X선 비탄성 산란 (RIXS) 연구에 따르면, 이러한 신호는 단일 마그논 산란 기작으로부터 나타날 수 있습니다. 본 연구에서는 라만 분광학 실험을 통해 $Y_2Ir_2O_7$의 단일 마그논 산란 현상을 설명하는 두 가지 스핀 해밀턴 모델을 발견했습니다. 타이트 바인딩 모형 분석을 사용하여 $Y_2Ir_2O_7$에 대한 올바른 스핀 해밀턴 모형의 매개변수를 규명하였습니다. 이 결과에서, 우리는 $Y_2Ir_2O_7$이 다른 파이로클로로 이리듐 산화물들의 위상과는 다른 위상학적 마그논 상태를 갖는다는 것을 발견했습니다. 해당 결과는 파이로클로로 이리듐 산화물 시스템이 마그논 위상을 설계하기에 좋은 플랫폼이며, 본 결과는 마그논의 위상학적 상태에 대한 다이어그램을 확정 짓는 데 중요한 단서입니다.

또한 상대론적 모트 절연 상태일 때 단일 마그논 산란 현상의 기작을 제시하였습니다. 강한 스핀-궤도 결합은 전자의 스핀과 각운동량이 얽힌 유사스핀 상태를 유도합니다. 유사스핀 상태의 궤도 각운동량 때문에, 전기 쌍극자 전환을 통해 마그논을 산란시킬 수 있습니다. 여기서, 우리는 파이로클로로 이리듐 산화물 시스템에서 단일 마그논 산란 메커니즘과 그들의 라만 텐서 대칭을 제시하였습니다. 우리의 결과는 4d/5d 유사스핀 물질의 단일 마그논 산란 현상과 라만 스펙트럼에 대한 이해도를 확장시켰습니다.

주요어: 강상관계 위상학적 상태, 전자 구조, 바일 반도체, 파이로클로로 이리듐 산화물.
학번: 2015-20332